Heat Release Rate Variations in Turbulent Syngas Spherical Cellular Flames at Elevated Pressures: Effect of Equivalence Ratio

K.K.J. Ranga Dinesh[1*], H. Shalaby[1], K.H. Luo[2], J.A. van Oijen[3], D. Thévenin[4]

1. Energy Technology Research Group, Faculty of Engineering and the Environment, University of Southampton, Southampton SO17 1BJ, UK.

2. Department of Mechanical Engineering, University College London, Torrington Place, London WC1E 7JE, UK.

3. Combustion Technology Group, Department of Mechanical Engineering, Eindhoven University of Technology, Den Dolech 2, 5612 AZ Eindhoven, Netherlands.

4. Laboratory of Fluid Dynamics and Technical Flows, University of Magdeburg "Otto von Guericke", Universitatsplatz 2, D-39106 Magdeburg, Germany.

[*] **Corresponding Author**: K.K.J. Ranga Dinesh, Energy Technology Research Group, Faculty of Engineering and the Environment, University of Southampton, Southampton, SO17 1BJ, UK.

Email: Dinesh.Kahanda-Koralage@soton.ac.uk

Tel: +44 (0) 2380598301

Manuscript Prepared for the submission of International Journal of Hydrogen Energy

October 2016

Abstract

Three-dimensional direct numerical simulations with detailed chemistry were conducted to investigate the effect of equivalence ratio on spatial variations of the heat release rate and flame markers of hydrogen/carbon monoxide syngas expanding spherical premixed flames under turbulent conditions at elevated pressures. The flame structures and the heat release rate were analysed in detail for fuel-lean, stoichiometric and fuel-rich centrally ignited spherical flames. The equivalence ratio changes the balance among thermo-diffuive effects, Darrieus-Landau instability and turbulence, leading to different flame dynamics and the heat release rate distribution, despite exhibiting similar cellular and wrinkling flames. The Darrieus-Landau instability is relatively insensitive to the equivalence ratio while the thermo-diffuive process is strongly affected by the equivalence ratio. As the thermo-diffusive effect increases as the equivalence ratio increases, the fuel-lean flame is more unstable than the fuel-rich flame with the stoichiometric flame in between, under the joint effects of the Darrieus-Landau instability and the thermo-diffusive effect. The local heat release rate and curvature display a positive correlation for the lean flame, no correlation for the stoichiometric flame, and negative correlation for the rich flame. Furthermore, the low and high heat release rate values for the fuel-lean flame are found in the negative and positive curvature zones, respectively, while the oppostite trends are found in fuel-rich flame. It is found that heat release rate markers based on species concentrations vary strongly with changing equivalence ratio. The results suggest that the HCO concentration and product of OH and CH_2O concentrations show good correlation with the local heat release rate for H_2/CO syngas-air stoichiometric flame under turbulent conditions at elevated pressures.

Key Words: Direct Numerical Simulation, Syngas Combustion, Elevated Pressure, Equivalence Ratio, Heat Release Rate Imaging, Flame Markers

Introduction

The growing concerns over the correlation between the global temperature and the carbon dioxide concentration in the atmosphere have prompted calls for increasing the use of low carbon fuels in future combustion engines [1-3]. Hydrogen and high hydrogen content (HHC) syngas fuel blends may become a major source of low carbon fuels. Fundamental and applied studies of hydrogen and syngas combustion characteristics have been widely conducted due to their practical relevance to clean combustion technologies. For example, many investigations into combustion characteristics of hydrogen and hydrogen-enriched syngas fuels have been reported for spark ignition internal combustion engine [4-7] and gas turbine combustor configurations [8]. These studies elucidated the general combustion characteristics of hydrogen and syngas fuels, as well as different mixture formation strategies and their emission characteristics. Detailed chemical kinetic mechanisms for hydrogen and syngas oxidation were also developed, for example [9-12]. In response to the interest in syngas combustion, several fundamental studies have been conducted on issues such as fuel variability and flame characteristics [13-14], flame blow out limits of syngas mixtures [15], laminar burning velocity [16-17] and high-pressure low-temperature ignition behaviour [18].

The aforementioned studies have revealed that the combustion characteristics and operability limits of HHC syngas flames differ considerably from those of conventional hydrocarbons. They have also highlighted several unresolved issues, particularly with respect to premixed combustion mode of HHC syngas fuels. One such an issue is the characterisation of heat release rate region (i.e. combustion intensity region) of HHC premixed syngas flames with respect to different fuel-air ratios in a high pressure environment, where combustion engines are generally operating. For example, increase in pressure reduces the flame thickness and triggers flame wrinkling at progressively smaller scales. This in turn can influence the local variation in the heat release rate. The complexity can be further increased with respect to equivalence ratio effects at elevated pressures [19]. Therefore, it is desirable to study the effects of equivalence ratio on combustion intensity of HHC syngas premixed flames at elevated pressures.

The local heat release rate (HRR) is generally expressed as:

$$Q = \sum_{k=1}^{N_s} h_k \dot{\omega}_k \tag{1}$$

where $\dot{\omega}_k$ ($kgm^{-3}s^{-1}$) and h_k (Jkg^{-1}) are the chemical mass production rate and species enthalpy of species k, and N_s is the total number of species involved in the oxidation processes.

Many experimental and numerical studies have been performed in fundamental configurations related to understanding spatial distribution of the local HRR in fuel-lean, stoichiometric and fuel-rich laminar and turbulent hydrogen and/or hydrogen-blended

hydrocarbon premixed flames at the atmospheric pressure. In most experiments carried out for traditional hydrocarbon premixed flames at the atmospheric pressure, the HRR has been estimated mainly via chemiluminescence measurements of radical species concentrations. For example, investigations by Najm et al. [20] revealed that the formyl radical (HCO) correlates very well with the HRR in laminar premixed flames. Furthermore, Paul and Najm [21] found that the product of hydroxyl (OH) and formaldehyde (CH_2O) images correlates well with the HRR in laminar premixed flames. Bockle et al. [22] also tested the applicability of the product of OH and CH_2O on estimating HRR in turbulent premixed flames and found that simultaneous imaging of OH and CH_2O correlates well with temperature measurements in turbulent Bunsen flames. Vagelopoulos and Frank [23] have demonstrated that the methylidyne radical (CH) follows heat release image reasonably well and can be used as a flame marker in undiluted methane flames at the stoichiometric condition. Various groups have also measured CH_2O and OH radicals and found that product of OH and CH_2O radicals correlates well with the HRR for turbulent premixed flames under various conditions including premixed flames approaching the blow-off conditions [24-27]. However, experiments are typically restricted to two-dimensional sections of the flame while the three-dimensional description of the flame generally requires three-dimensional numerical simulations.

Several numerical modelling studies have been performed to study HRR in turbulent hydrocarbon, hydrogen and/or hydrogen-enriched hydrocarbon premixed flames at the atmospheric pressure. Particularly, Direct Numerical Simulations (DNS), in which the

governing equations are fully resolved down to the Kolmogorov length scales, have been successfully conducted to reveal the HRR patterns of various fuel/air mixtures at the atmospheric pressure. For example, Baum et al. [28] analysed DNS results of peak radical concentrations relative to peak heat release in turbulent $H_2/O_2/N_2$ flames over a range of equivalence ratios ranging from 0.35 (fuel-lean mixture), 1.0 (stoichiometric mixture) to 1.3 (fuel-rich mixture). They found that heat release and hydrogen peroxide (H_2O_2) contours remain thin and connected over a range of equivalence ratio considered. They also observed transition of heat release rate patterns from fuel-lean cases to fuel-rich cases. Echekki and Chen [29] performed DNS and evaluated the effects of strain rate and curvature on the intermediate radical concentrations and heat release for premixed methane-air flames. They found that faster diffusing intermediate species, such as H and H_2, link intensely with flame curvature and also reflected in the heat release rates. DNS results reported by Im and Chen [30] have demonstrated that the preferential diffusion (non-unity Lewis number effects) influences the maximum heat release rate in rich-rich mixture and lean-lean mixture interacting premixed hydrogen flames. They have also demonstrated that the heat release rate is intensified near the flame cusp region that is concave toward the fresh mixture for the rich-rich mixture with equivalence ratio 2.0, while heat release rate is weakened near the cusp region for the lean-lean mixture with equivalence ratio 0.4. Later, Hawkes and Chen [31] performed DNS of hydrogen blended lean-premixed methane flames with equivalence ratio 0.52 and demonstrated that the volumetric heat release is increased due to hydrogen-enrichment as well as turbulence stretch effects. Wang et al. [32] studied hydrogen-air swirling premixed flames with equivalence ratios 0.6 and 1.0 using DNS. They found that the heat release in the

stoichiometric swirling flame is higher than the fuel-lean swirling flame. Recently, Nikolaou and Swaminathan [33] re-examined the validity of radical species HCO as a reliable HRR marker with respect to stoichiometric and lean combustion of methane-air mixtures and for hydrogen-enriched multi-component fuel-air mixtures using DNS data. Their analysis suggests that the product of H and CH_2O correlates better with the HRR for low and high turbulence levels compared to the product of OH and CH_2O. Although the aforementioned experimental and DNS studies provide valuable insights into the local variation of the HRR and flame markers at the atmospheric pressure, unsteady HRR patterns and suitable flame markers at the elevated pressures are still not well established.

In the light of the above observations, the objective of this study is to investigate the local heat release rate of HHC syngas-air mixtures at elevated pressures and examine how commonly used flame markers correlate with the HRR over a range of equivalence ratios changing from fuel-lean to stoichiometric to fuel-rich mixtures under turbulent conditions. For this we have performed three-dimensional DNS using complex chemistry and the mixture-averaged transport model (non-unity Lewis number model) including the Soret effect (thermal diffusion). The present study is part of a larger effort to identify the flame characteristics of hydrogen and syngas combustion of both non-premixed and premixed combustion modes at the atmospheric and high pressure conditions. Our earlier three-dimensional direct numerical and large eddy simulations focused on the fundamental burning issues of turbulent non-premixed flames over a wide range of flow conditions and syngas mixtures at the atmospheric pressure [34-40]. Our very recent three-dimensional DNS investigated different aspects of HHC turbulent premixed flames

from low to high initial turbulence levels at elevated pressures [41, 42]. It is noted that in a previous DNS study of the preferential diffusion effects on lean premixed syngas flames at elevated pressures [41], it was found that the thermo-diffusive instability greatly influences the cellular flame front wrinkling of the lean premixed syngas flame due to strong preferential diffusion effects when it develops under low initial turbulence level at elevated pressures. The study also found that the thermo-diffusive instability effects are destabilising and preferential diffusion is overwhelmed by turbulent mixing for the lean premixed syngas flame when it develops under high initial turbulence level at elevated pressures. We also found small and large scale wrinkling structures that develop over the flame surface of a lean premixed syngas flame increase its area and thereby the global propagation speed at elevated pressures compared to those at the atmospheric pressure [42]. The following sections will describe numerical methods and simulation details and results. The final section presents conclusions.

Numerical methods and simulation details

To investigate the effects of equivalence ratio on variation in the spatial distribution of the HRR at elevated pressure of p=4bar, three DNS test cases of turbulent expanding spherical flames ranging from fuel-lean to stoichiometric to fuel-rich combustion were performed. Three equivalence ratios selected were 0.7 (lean flame), 1.0 (stoichiometric flame) and 1.4 (rich flame), respectively. In all three cases considered here, DNS was performed for HHC premixed H_2/CO syngas fuel mixture with 70% of H_2 and 30% of CO by volume. In all DNS test cases, the turbulent Reynolds number (Re_t) based on initial turbulence velocity fluctuations and the integral length was set to 100.

For the present DNS cases, the parallel DNS flame solver Parcomb [43-45] is used. Parcomb solves the fully compressible transport equations on a uniform Cartesian grid for mass, momentum, total internal energy, and the mass fraction of chemical species using detailed transport properties. In this study, we employ the mixture-averaged transport model (non-unity Lewis number model) supplemented with a model for Soret effect (thermal diffusion) to compute the diffusive process. It is important to note that the Soret effect is considered to be vital in situations where light radicals such as H or H_2 are present, in particular for HHC syngas combustion. To compute the diffusion velocities, one has to accurately determine the binary coefficient via the diffusion matrix, which is computationally expensive. In this study, we adopt the Hirschfelder-Curtiss approach [46], whereby an appropriate diffusion coefficient is obtained via binary diffusion coefficient.

Spatial derivatives are obtained using a sixth order central difference scheme which gradually reduces to a fourth order central difference scheme near boundaries. Time integration is achieved using a fourth order Runge–Kutta scheme. A Courant-Friedrichs-Levy (CFL) condition for the convective terms and a Fourier condition pertaining to the diffusion terms are imposed to ensure the stability of the explicit integration and determine a suitable time step. As in previous DNS studies of high pressure combustion [41, 42], improved non-reflecting inflow/outflow Navier-Stokes characteristics boundary conditions (NSBC) are applied in analogy with the pressure relaxation [47]. The initial isotropic turbulent velocity field for each case was initialised using a combined approach

of digital filtering (DF) [48] and random noise diffusion [49]. The flame chemistry is represented by the H_2/CO kinetic scheme developed by Goswami et al. [50, 51]. This reaction model incorporates the thermodynamic, kinetic, and species transport properties related to H_2 and CO oxidation at elevated pressures, consisting of 14 species (O, O_2, N_2, H, H_2, H_2O, OH, H_2O_2, HO_2, CO, CO_2, HOCO, HCO, CH_2O) and 52 individual reactions. Readers are referred to [41, 42] for details of the governing equations and the mixture-averaged transport model.

Fig. 1 shows the computational domain of the expanding spherical flame. The cubic domain has a length of 8.0×10^{-3}m on each side. A time step of approximately 6.0×10^{-9}s was used for all simulations. The initial hot spherical laminar flame kernel is constructed at the center of the computational domain with initial radius of $r_0 = 0.6$mm. The physical and numerical parameters used in the present study are listed in Table 1, where l_t is the integral length scale measured directly from the initial turbulence field, u' the rms velocity fluctuation, S_L the laminar flame speed, $\mathrm{Re}_t = u' l_t / \nu$ the turbulent Reynolds number, $\delta_{th} = (T_b - T_u)/\max|\nabla T|$ the laminar thermal flame thickness with T_b and T_u being the burnt and fresh gas temperatures, $Da = (l_t / u')/(\delta_{th} / S_L)$ the Damköhler number, $Ka = [(u'/S_L)^3/(l_t/\delta_{th})]^{0.5}$ the Karlovitz number. A fresh gas temperature of $T_u = 300K$ is considered. Since the focus in this work is on the influence of equivalence ratio on combustion intensity, we have used nearly identical initial turbulence field for each flame. Each set up is superimposed with a homogeneous isotropic turbulent field at t=0 with $u' \approx 1.1$ m/s. It is noted that

u'/S_L shows different values for different cases in Table 1 due to increase in laminar burning velocity when the fuel-air mixture changes from lean to stoichiometric to rich conditions. For the H_2/CO syngas fuel mixture with 70% of H_2 and 30% of CO at a pressure value of 4 atm, the laminar burning velocity, $S_L \approx 0.53, 0.76$ and 0.86 m/s for equivalence ratios of 0.7, 1.0 and 1.4, respectively. From the calculation of turbulence intensity u'/S_L and length-scale ratio l_t/δ_{th} , it can be concluded that the flames considered here fall within the Thin Reaction Zone (TRZ).

To gain an understanding of the effect of grid resolution on the DNS results at elevated pressures, simulations were conducted for the lean mixture case using three different Cartesian grids with $400\times400\times400$, $600\times600\times600$ and $800\times800\times800$ points. Overall, the HRR plots obtained from three different grids indicate that a Cartesian grid with $600\times600\times600$ grid points produces grid-independent results for the simulated flame at a pressure value of 4 atm. Results of the grid-independent analysis are provided in [41, 42].

Results and discussion

In this section, the results of the simulations will be presented. The objective is to discuss the effect of equivalence ratio on local HRR of HHC syngas premixed flames, and identify appropriate flame markers which correlate with the HRR, ideally as much

linearly as possible at elevated pressures. For this, first we discuss the effect of equivalence ratio on intrinsic flame instabilities, cellular flame structures, and spatial distribution of the HRR. Next we assess the effect of equivalence ratio on reliable chemical markers based on radical species concentrations that correlate well with the HRR.

Effect of equivalence ratio on heat release rate variation

To identify the effect of equivalence ratio on evolution of flame wrinkling at elevated pressures, we compare the transient flame development among the flames. Fig. 2 shows the sequences of images of lean, stoichiometric and rich expanding spherical flames at 4 atm. The DNS images demonstrate that the three flames exhibit nearly identical flame morphology at the very early stage, but they become heavily wrinkled and showing differences at the later stage. To study the effect of equivalence ratio on flame acceleration at elevated pressures, we observe all the three flames developing to a fixed surface area corresponding to the flame front isotherm value. We calculate the flame surface area at the flame front with respect to flame isotherms of T=1240K, 1308K and 1275K for lean, stoichiometry and rich flames. It is seen that at the late stage (bottom images of Fig. 2), the time taken by the lean flame to develop to a fixed flame surface area (5.685e-5 m^2) is t=1.35e-4s while its value for stoichiometric and rich flames are t=1.48e-4s and t=1.63e-4s, respectively. This is due to the fact that the three flames accelerate at different rates due to different levels of relative turbulence u'/S_L.

Given the nature of cellular burning structures over the flame surface (Fig. 2), it is of interest to assess the effect of equivalence ratio on the magnitude of flame wrinkling at elevated pressures. The magnitude of flame wrinkling can be evaluated using curvature which marks the direction of the gradient scalars within the flame and is mainly coupled with the diffusion rates of heat and mass. Fig. 3 shows iso-surfaces of the flame front coloured by local curvature. Fig. 3 demonstrates that all the three flames are wrinkled with appearance of small scale convex and concave structures superimposed with large scale flame branches. To further identify the effect of equivalence ratio on the formation of small and large scale wrinkling structures at elevated pressures under turbulent conditions, we plot a zoom view over a selected region in Fig. 3. In Fig. 4, for the lean flame, interestingly, a zoom view region shows a strongly wrinkled surface with more prominent convex structures than concave structures. The convex structures protrude into the unburned reactants and expand the effective contact surface between the flame front and unburned reactants. For the stoichiometric flame, a zoom view region still shows similar small scale convex and concave structures, which are weaker than those of the lean flame. Furthermore, the zoomed view of the rich flame shows even weaker small scale structures compared to both lean and stoichiometric flames. It is important to note that these findings are consistent with hydrogen/air and syngas/air experimental observations reported in [52-55]. Together, Figs. 3 and 4 indicate much more convex structures than concave ones on the flame front for all the three flames which reveals a common feature of turbulent premixed flames at elevated pressures [56].

To further investigate the curvature effects on flame wrinkling at different equivalence ratio in high pressure environment, we plot histogram and probability density function (pdf) of curvature for lean, stoichiometric and rich flames. Fig. 5 shows histograms and the true pdf curve (green-line) and Gaussian pdf curve (red-line) for lean, stoichiometric and rich flames, respectively. The most prominent feature of the curvature histograms is the more symmetrical distribution with a peak at zero curvature value for the lean flame, and a more asymmetric distribution biased toward negative curvature values for the rich flame. Furthermore, the pdf of curvature displays long-tailed negative and positive curvature values for the lean flame. In contrast, of the tail on the positive curvature side is very short for the rich flame.

It is known that centrally ignited flames are subjected to Thermo-Diffusive (TD) instability as a result of strong preferential diffusion (non-unity Lewis number) effects, and Darrieus-Landau (DL) instability resulting from thermal expansion [52-55]. The DL instability is particularly dominant in large scale wrinkling structures while the TD instability is mainly responsible for the small scale wrinkling structures. In premixed flames propagating under turbulent conditions at elevated pressures, the flame front wrinkling is affected by both turbulence and intrinsic flame instabilities like DL-TD instabilities [41, 55, 56].

To assess the quantitative effect of TD and DL instabilities on cellular flame front growth rate for the three flames, we discuss the instability plots between each flame. In our earlier work, we assessed the onset of instabilities in response to preferential diffusion for

the lean premixed flame under low and high turbulence levels at elevated pressures [41]. Details of the mathematical expressions for the growth rate, contribution to the growth rate of the TD instability, contribution to the growth rate of the DL instability can be found in [41]. The effective Lewis number Le_{eff} appears in those mathematical expressions in ref. [41] depends on equivalence ratio and defined here as the combination of the fuel and oxidiser Lewis numbers [57].

$$Le_{eff} = \frac{Le_D + \mathrm{A}Le_E}{1+\mathrm{A}}, \qquad \mathrm{A} = \begin{cases} 1+\beta(\phi^{-1}-1) & \phi < 1 \\ 1+\beta(\phi-1) & \phi > 1. \end{cases} \tag{2}$$

where Le_E and Le_D are the Lewis number of excessive and deficient reactants, respectively. Based on the parameters presented in Table 2, the effective Lewis number is calculated from Eq. (2) corresponding to each mixture. Figure 6 illustrates the TD instability, DL instability, and growth rate as a function of the wave number for equivalence ratios of 0.7, 1.0 and 1.4. It is evident that for the lean flame, the TD curve shows nearly zero values at small wavenumbers but slightly negative values at large wavenumbers, indicating that the thermodiffusive effect is stabilising overall. For the stoichiometric and rich flames, the TD curves show strong negative values especially with increasing wave number, implying that the TD influence is stabilising. On the other hand, the DL instability curves show positive values for all the three flames with nearly identical distributions. A small difference in the DL curve between each flame is associated with a small variation in the thermal expansion coefficient (Table 2). For all the three flames, the results indicate that the DL effects are destabilising. In general, the trends observed from the instability plots in Fig. 6 confirm that the lean flame is more unstable than the stoichiometric flame which is in turn more unstable than the rich flame,

under the joint actions of DL ad TD effects. It is noted that while TD instability is suppressed in the rich mixture due to the higher Lewis number, pulsating instability, which is thermal diffusive in nature, can be activated in sufficiently off-stoichiometric rich mixtures ($\phi \geq 1.3$) with increasing positive stretch [58]. This in turn can couple with other instabilities and alter quantities of interest such as mass burning rate in the rich mixture.

Since our primary aim is to assess the effect of equivalence ratio on local HRR, we now study the detailed spatial distribution of the heat release along a flame front. Fig. 7 shows iso-surface contours of instantaneous HRR for three equivalence ratios at 4 atm. The iso-surface contours of instantaneous HRR show noticeable differences in the spatial distribution of the HRR with respect to varying equivalence ratio. The flame front of the lean flame is much thinner and more wrinkled compared to those of the stoichiometric and rich flames. For the lean flame, the most distinct feature is the small HRR and even flame quenching in some local areas along the flame front. It is seen that these areas coincide with small scale concave (or cusps) structures protruding into the burned mixture. To further visualise this behaviour, we plotted zoomed-in view of selected regions in Fig. 8. Together, Figs. 7 and 8 suggest that, for the lean flame, weak burning structures are formed in regions of strong negative curvatures. Flame holes can also appear in some cusps. For the stoichiometric flame, similar trends are found except that there are no holes in the flame front.. For the rich flame, intense burning is observed along the flame front, which remains thick and continuous, even in the regions of cusps

structures. This behaviour was also observed in the previous DNS work by Im and Chen [30] for the rich hydrogen premixed flame at the atmospheric pressure.

Together, Figs. 7 and 8 indicate that convex structures associated with positive curvatures and concave structures associated with negative curvatures lead to very different flame behaviours and consequently quite different values of of the HRR. To shed more light into the effects of local negative and positive curvature values on the HRR at different equivalence ratios, the scattered HRR versus curvature along the instantaneous flame front are plotted in Fig. 9 for lean, stoichiometric and rich flames. Significantly, the results of lean, stoichiometric and rich flames show noticeable differences. For the lean flame, lower HRR values are found in negative curvature regions, unsurprisingly. For example, for the lean flame, the lowest local HRR (3.5e+10 W/m^3) occurs in the negative curvature zone with curvature of approximately -20000 1/m. Such a region is close to local flame extinction along the flame front. Furthermore, for the lean flame, the best-fit curve shows positive correlation between curvature and HRR with high HRR values in the positive curvature zone and low HRR values in the negative curvature zone. This is an important finding. On the other hand, for the stoichiometric flame, the best-fit curve shows no obvious correlation between curvature and HRR. Finally, for the rich flame, the best-fit curve indicates negative correlation between curvature and HRR. Interestingly, it shows an increase in HRR in the negative curvature zone and decrease in HRR in the positive curvature zone, in agreement with the coutour plots in Figs. 7 and 8. For example, for the rich flame, the highest local HRR (2.48e+11 W/m^3) occurs in the negative curvature zone with curvature of approximately –50000 1/m while lowest value

(5e+10 W/m^3) exhibits in the positive curvature zone with curvature of approximately 50000 1/m. Interestingly, similar trends were also reported by Ayoola et al. [24] in their experiment carried out for turbulent premixed flames with Lewis numbers are greater than unity at the atmospheric pressure. One possible explanation is: in the rich flame, the convex areas of positive curvature on the reactant side the mixture is too rich to burn fast; the concave areas of negative curvature on the product side have high temperature and still sufficient fuel available to burn. This explanation can be extended both the lean and stoichiometric flames too. In the lean flame, the concave regions on the product side simply have a lack of fuel to burn, so its HRR is lower than that on the reactant side. For the stoichiometric flame, the two factors, temperature and availability of fuel, in the positive and negative curvature regions balance each other, so that the HRR and curvature appear to be uncorrelated.

Effects of equivalence ratio on heat release rate markers

In this section we discuss the effect of equivalence ratio on heat release rate markers at elevated pressures. Given our understanding of well-known HRR markers of premixed flames such as HCO and product of OH and CH_2O for combustion at the atmospheric pressure [20-22, 33], it is natural to ask, how reliable these HRR markers are for multi-component syngas fuel flames at elevated pressures? It is not entirely clear whether species such as HCO and product of OH and CH_2O are linearly correlated with heat release under turbulent conditions at elevated pressures due to two major reasons: the first reason is effects of curvature and strain rates induced by large scale wrinkling as a result of turbulence, and fine scale wrinkling as a result of flame intrinsic instability, the

second reason is the molecular structure effects on the oxidation of chemistry. It is noted that the second issue is even more important for high hydrogen content fuel mixtures such as H_2/CO syngas because preferential diffusion effects can play a role in molecular diffusion [41]. In addition to these two reasons, the correlations can also be influenced by the equivalence ratio. Turning now to study this question, we analyse scatter plots of the normalised HRR with the normalised mass fractions of HCO and product of normalised mass fractions of OH and CH_2O at 4 atm.

Fig. 10 shows the normalised HRR against the normalised mass fraction of HCO for lean, stoichiometric and rich flames at 4 atm. The most striking observation from Fig. 10 is the occurrence of linear spatial correlation between HRR and HCO concentration for the stoichiometric flame. This finding confirms that HCO can be used as a reliable HRR marker for the stoichiometric premixed H_2/CO syngas turbulent flame at elevated pressures. For the lean flame, it shows a poor correlation with the HRR with more scatter at higher HCO concentrations. Finally, for the rich flame, there are two regimes separated by the HCO mass fraction of 0.5. In each regime, there appears to be a linear correlation between HRR and HCO concerntration.

The normalised HRR against the product of normalised mass fractions of OH and CH_2O at 4 atm is given in Fig. 11. Despite small differences, the scatter plots show the same trends for the lean, stoichiometric and rich flames. Importantly, the HRR correlates positively with the product of mass fractions of OH and CH2O over the full range of values, despite an inflection point at a value of around 0.15 for the product of mass fractions of OH and CH2O. If the purpose of a flame marker is a qualitative indicator of

the chemical reaction rate, then the product of OH and CH2O mass fractions is a good flame marker, because it is relatively insensitive to the equivalence ratio.

Conclusions

A three-dimensional direct numerical simulation study on the effect of equivalence ratio on the spatial distribution of the heat release rate and heat release markers of syngas-air expanding spherical premixed flames was conducted under turbulent conditions at elevated pressures. Simulations were performed using detailed syngas chemistry validated at high pressures. The diffusive processes were computed using the mixture-averaged transport models (non-unity Lewis number model) including the Soret effect. Three cases with equivalence ratios of 0.7, 1.0 and 1.4, respectively, were performed for HHC premixed H_2/CO syngas fuel mixture with 70% of H_2 and 30% of CO by volume at initial pressure value of p = 4 bar and initial turbulent Reynolds number of Re_t = 100. The main conclusions of the study are as follows:

1. Centrally ignited flame balls are subjected to the influence of thermo-diffuive effects, Darrieus-Landau instability and turbulence, whose flame surfaces exhibit cellular and wrinkling structures to varying degrees. The equivalence ratio introduces additional complexity which affects the flame surface dynamics and

the heat release rate (HRR). The Darrieus-Landau instability is relatively insensitive to the equivalence ratio while the thermo-diffuive process is strongly affected by the equivalence ratio. Under the turbulent and elevated pressure conditions simulated, the thermo-diffusive effect is stabilising especially at high wavenumbers while Darrieus-Landau instability is destabilising over the full range of wavenumbers. As the thermo-diffusive effect increases as the equivalence ratio increases, the (fuel) lean flame is more unstable than the (fuel) rich flame with the stoichiometric flame in between, under the joint effects of the Darrieus-Landau instability and the thermo-diffusive effect. Flame holes appear in the cusps of the fuel-lean flame, indicating local flame quenching, which is not found in the stoichiometric and fuel-rich flames.

2. The equivalence ratio has a significant impact on the spatial distribution of HRR. For the lean flame, a positive correlation is found between curvature and HRR with low HRR values in the negative curvature zone and high HRR values in the positive curvature zone. The opposite trends are found in the rich flame. For the stoichiometric flame, no apparent correlation is found between curvature and heat release rate. These outcomes are due to the changing balance of two key factors, temperature and availability of fuel, in the positive and negative curvature regions as the equivalence ratio increases.
3. The equivalence ratio has a complex relation with the common flame markers. Scatter plots of HRR versus the mass fraction of key species concentrations show that HCO concentration is linearly correlated with HRR for the stoichiometric flame. For both fuel lean and rich combustion, however, the relation between

HCO concentration and HRR is far from linearity. On the other hand, scatter plots of the HRR versus the product of mass fractions of OH and CH2O show the same trends regardless of the equivalence ratio. Importantly, their correlations are positive over the full range of values, despite an inflection point. The product of OH and CH2O mass fractions is therefore a better flame marker than HCO, but its calculation is more involved.

Acknowledgements

This work was sponsored by the Engineering and Physical Sciences Research Council (EPSRC), under the grant EP/L025051/1 (High Hydrogen Content Fuel Burning at High Pressure). Computing resources on UK National Supercomputer ARCHER funded by the EPSRC grant No. EP/J016381/2 are gratefully acknowledged.

References

1. Sanchez AL, Williams FA. Recent advances in understanding of flammability characteristics of hydrogen. Prog Energy Combust Sci 2014; 41: 1-55.

2. Heidenreich S, Foscolo PU. New concepts in biomass gasification. Prog Energy Combust Sci 2015; 46: 72-95.

3. Sarathy SM, Obwald P, Hansen N, Kohse-Hoinghaus K. Alcohol combustion chemistry. Prog. Energy Combust Sci 2014; 44: 40-102.

4. White CM, Steeper RR, Lutz AE. The hydrogen-fueled internal combustion engine: a technical review. Int J Hydrogen Energy 2006; 31: 1292-1305.

5. Verhelst S, Wallner T. Hydrogen-fueled internal combustion engines. Prog Energy Combust Sci 2009; 35: 490-527.

6. Shivapuji AM, Dasappa S. In-cylinder investigations and analysis of a SI gas engine fuelled with H_2 and CO rich syngas fuel: Sensitivity analysis of combustion descriptors for engine diagnostics and control. Int J Hydrogen Energy 2014; 39: 15786-15802.

7. Hagos FY, Aziz ARA, Sulaiman SA, Syngas (H_2/CO) in a spark-ignition direct-injection engine. Part 1: Combustion, performance and emissions comparison with CNG. Int J Hydrogen Energy 2014; 39: 17884-17895.

8. Sorgenfrei M, Tsatsaronis G. Detailed exergetic evaluation of heavy-duty gas turbine systems running on natural gas and syngas. Energy Conv Manag 2016; 107: 43-51.

9. Boehman AL, Corre OL. Combustion of syngas in internal combustion engines. Combust. Sci and Tech 2008; 180: 1193-1206.

10. Chaos M, Dryer FL. Syngas combustion kinetics and applications. Combust Sci and Tech 2008; 180: 1053-1096.

11. Hanna J, Lee WY, Shi Y, Ghoniem AF. Fundamentals of electro-and thermochemistry in the anode of solid-oxide fuel cells with hydrocarbon and syngas fuels. Prog Energy Combust Sci 2014; 40: 74-111.

12. Konnov AA. On the role of excited species in hydrogen combustion. Combust Flame 2015; 162: 3755-3772.

13. Ranga Dinesh KKJ, Jiang X, van Oijen JA, Bastiaans RJM, de Goey LPH. Influence of fuel variability on the characteristics of impinging non-premixed syngas burning. Proc Combust Inst 2013; 34: 3219-3229.

14. Ranga Dinesh KKJ, Luo KH, Kirkpatrick MP, Malalasekera W. Burning syngas in a high swirl burner: effects of fuel composition. Int J Hydrogen Energy 2013; 38: 9028-9042.

15. Sayad P, Schonborn A, Klingmann J. Experimental investigations of the lean blowout limit of different syngas mixtures in an atmospheric, premixed, variable swirl burner. Energy Fuels 2013; 27: 2783-2793.

16. Zhang W, Gou X, Kong W, Chen Z. Laminar flame speeds of lean high-hydrogen syngas at normal and elevated pressures. Fuel 2016; 181: 958-963.

17. Li HM, Li GX, Sun ZY, Zhai Y, Zhou ZH. Measurements of the laminar burning velocities and markstein lengths of lean and stoichiometric syngas premixed flames under various hydrogen fractions. Int J Hydrogen Energy 2014; 39: 17371-17380.

18. Mansfield AB, Wooldridge MS. High-pressure low-temperature ignition behaviour of syngas mixtures. Combust Flame 2014; 161: 2242-2251.

19. Wei ZL, Leung CW, Cheung CS, Huang ZH. Effects of equivalence ratio, H_2 and CO_2 addition on the heat release characteristics of premixed laminar biogas-hydrogen flame. Int J Hydrogen Energy 2016; 41: 6567-6580.

20. Najm HN, Paul PH, Mueller CJ, Wyckoff PS. On the adequacy of certain experimental observables as measurements of flame burning rate. Combust Flame 1998; 113: 312-332.

21. Paul PH, Najm HN. Planer laser-induced fluorescence imaging of flame heat release rate. Sympo (Int) on Combustion 1998; 27: 43-50.

22. Bockle S, Kazenwadel J, Kunzelmann T, Shin DI, Schulz C, Wolfrum J. Simultaneous single-shot laser-based imaging of formaldehyde, OH, and temperature in turbulent flames. Proc Combust Inst 2000; 28: 279-286.

23. Vagelopoulos CM, Frank JH. An experimental and numerical study on the adequacy of CH as a flame marker in premixed methane flames. Proc Combust Inst 2005; 30: 241-249.

24. Ayoola BO, Balachandran R, Frank JF, Mastorakos E, Kaminski CF. Spatially resolved heat release rate measurements in turbulent premixed flames. Combust Flame 2006; 144 : 1-16.

25. Vena PC, Deschamps B, Guo H, Smallwood GJ. Heat release rate variations in a globally stoichiometric, stratified iso-octane/air turbulent V-flame. Combust Flame 2015; 162: 944-959.

26. Kariuki J, Dowlut A, Yuan R, Balachandran R, Mastorakos E. Heat release imaging in turbulent premixed methane-air flames close to blow-off. Proc Combust Inst 2015; 35: 1443-1450.

27. Mulla IA, Dowlut A, Hussain T, Nikolaou ZM, Chakravarthy SR, Swaminathan N, Balachandran R. Heat release rate estimation in laminar premixed flames using laser-induced fluorescence of CH_2O and H-atom. Combust Flame 2016; 165: 373-383.

28. Baum M, Poinsot TJ, Haworth DC, Darabiha N. Direct numerical simulation of $H_2/O_2/N_2$ flames with complex chemistry in two-dimensional turbulent flows. J Fluid Mech 1994; 281: 1-32.

29. Echekki T, Chen JH. Unsteady strain rate and curvature effects in turbulent premixed methane-air flames. Combust Flame 1996; 106: 184-202.

30. Im HG, Chen JH. Preferential diffusion effects on the burning rate of interacting turbulent premixed hydrogen-air flames. Combust Flame 2002; 131: 246-258.

31. Hawkes ER, Chen JH. Direct numerical simulation of hydrogen-enriched lean premixed methane-air flames. Combust Flame 2004; 138: 242-258.

32. Wang H, Luo K, Qiu K, Lu S, Fan J, A DNS study of hydrogen/air swirling premixed flames with different equivalence ratios. Int J. Hydrogen Energy 37 (2012) 5246-5256.

33. Nikolaou ZM, Swaminathan N. Heat release rate markers for premixed combustion. Combust Flame 2014; 161: 3073-3084.

34. Ranga Dinesh KKJ, Jiang X, van Oijen JA. Numerical simulation of hydrogen impinging jet flame using flamelet generated manifold reduction. Int J Hydrogen Energy 2012; 37: 4502-4515.

35. Ranga Dinesh KKJ, Jiang X, Kirkpatrick MP, Malalasekera W. Combustion characteristics of H_2/N_2 and H_2/CO syngas nonpremixed flames. Int J Hydrogen Energy 2012; 37: 16186-16200.

36. Ranga Dinesh KKJ, Jiang X, van Oijen JA, Bastiaans RJM, de Goey LPH. Hydrogen-enriched nonpremixed jet flames: effects of preferential diffusion. Int J Hydrogen Energy 2013; 38: 4848-4863.

37. Ranga Dinesh KKJ, Jiang X, van Oijen JA. Hydrogen-enriched non-premixed jet flames: compositional structures with near-wall effects. Int J Hydrogen Energy 2013; 38: 5150-5164.

38. Ranga Dinesh KKJ, Jiang X, van Oijen JA. Hydrogen-enriched non-premixed jet flames: analysis of the flame surface, flame normal, flame index and Wobbe index. Int J Hydrogen Energy 2014; 39: 6753-6763.

39. Ranga Dinesh KKJ, Jiang X, van Oijen JA. Near-field local flame extinction of oxy-syngas non-premixed jet flames: a DNS study. Fuel 2014; 130: 189-196.

40. Ranga Dinesh KKJ, van Oijen JA, Luo, KH, Jiang X. Nitric oxide pollutant formation in high hydrogen content (HHC) syngas flames. Int J Hydrogen Energy 2015; 40: 13621-13634.

41. Ranga Dinesh KKJ, Shalaby H, Luo KH, van Oijen JA, Thévenin D. High hydrogen content syngas fuel burning in lean premixed spherical flames at elevated pressures: effects of preferential diffusion. Int J Hydrogen Energy 2016; 41: 18231-18249.

42. Ranga Dinesh KKJ, Shalaby H, Luo KH, van Oijen JA, Thévenin D. Effects of pressure on cellular flame structure of high hydrogen content lean premixed syngas spherical flames: A DNS study. Int J Hydrogen Energy 2016, Submitted.

43. Hilbert R, Thévenin D. Autoignition of turbulent non-premixed flames investigated using direct numerical simulations. Combust Flame 2002; 128: 22–37.

44. Hilbert R, Tap F, El-Rabii H, Thévenin D. Impact of detailed chemistry and transport models on turbulent combustion simulations. Prog Energy Combust Sci 2004; 30: 165–193.

45. Fru G, Janiga G, Thévenin D. Impact of volume viscosity on the structure of turbulent premixed flames in the thin reaction zone regime. Flow Turb Combust 2012; 88: 451-478.

46. Hirschfelder J, Curtiss C, Bird R. Molecular Theory of Gases and Liquids. Wiley, New York 1954.

47. Yoo CS, Im HG. Characteristic boundary conditions for simulations of compressible reacting flows with multi-dimensional, viscous and reaction effects. Combust Theory Model 2007; 11: 259-286.

48. Klein M, Sadiki A, Janicka J. A digital filter based generation of inflow data for spatially developing direct numerical or large eddy simulations. J Comput Phys 2003; 186: 652–665.

49. Kempf A, Klein M, Janicka J. Efficient generation of initial and inflow conditions for transient turbulent flows in arbitrary geometries. Flow Turb Combust 2005; 74: 67–84.

50. Goswami M, Bastiaans RJM, Konnov AA, de Goey LPH. Laminar burning velocity of lean H_2-CO mixtures at elevated pressure using the heat flux method. Int J Hydrogen Energy 2014; 39: 1485-1498.

51. Goswami M, van Griensven JGH, Bastiaans RJM, Konnov AA, de Goey LPH. Experimental and modelling study of the effect of elevated pressure on lean high-hydrogen syngas flames. Proc Combust Inst 2015; 35: 655-662.

52. Law CK, Jomaas G, Bechtold JK. Cellular instabilities of expanding hydrogen/propane spherical flames at elevated pressures: theory and experiment. Proc Combust Inst 2005; 30: 159-167.

53. Yuan J, Ju Y, Law CK. On flame-front instability at elevated pressures. Proc Combust Inst 2007; 31: 1267-1274.

54. Vu TM, Park J, Kwon OB, Bae DS, Yun JH. Effects of diluents on cellular instabilities in outwardly propagating spherical syngas-air premixed flames. Int J Hydrogen Energy 2010; 35: 3868-3880.

55. Wang J, Xie Y, Cai X, Nie Y, Peng C, Huang Z. Effect of H_2O addition on the flame front evolution of syngas spherical propagation flames. Combust Sci Tech 2016; 188: 1054-1072.

56. Wang J, Zhang M, Huang Z, Kudo T, Kobayashi H. Measurement of the instantaneous flame front structure of syngas turbulent premixed flames at high pressure. Combust Flame 2013; 160: 2434-2441.

57. Frouzakis CE, Fogla N, Tomboulides AG, Altantzis C, Matalon M. Numerical study of unstable hydrogen/air flames: shape and propagation speed. Proc Combust Inst 2015; 35: 1087-1095.

58. Christiansen EW, Law CK. Pulsating instability and extinction of stretched premixed flames. Proc Combust Inst 2002; 29: 61-68.

Table 1: Turbulence and flame properties at three equivalence ratios at the beginning of the simulation. Note that pressure is constant during the simulation.

Equivalence ratio (ϕ)	0.7	1.0	1.4
Pressure (atm)	4 atm	4 atm	4 atm
Turbulent Reynolds number (Re_t)	100	100	100
Damköhler number (Da)	2.99	3.57	3.82
Karlovitz number (Ka)	3.33	2.54	1.15
Kinematic viscosity ($\nu,\ m^2/s$)	4.13e-06	4.20e-06	4.31e-06
Integral length scale (l_t, m)	6.37e-04	6.37e-04	6.37e-04
u'/S_L	2.07	1.45	1.27
l_t/δ_{th}	6.05	6.05	6.05
Grid resolution	$600\times600\times600$	$600\times600\times600$	$600\times600\times600$

Kolmogorov length scale (η_k, μm)	14.9	14.9	14.9
Cell width (μm)	13	13	13
Number of grid points in flame thickness	8	8	8

Table 2: Data used to compute the theoretical relation of thermo-diffusive instability, Darries-Landau instability and growth rate extracted from the simulations.

ϕ	σ	β	$Le_{H_2/CO}$	Le_O	Le_{eff}
0.7	6.8	8.0	0.385	2.3	0.784
1.0	6.95	5.2	0.43	2.3	1.365
1.4	6.85	3.98	0.49	2.3	1.791

ϕ - equivalence ratio

σ - thermal expansion parameter

β - Zeldovich number

$Le_{H_2/CO}$ - fuel Lewis number

Le_O - oxidiser Lewis number

Le_{eff} - effective Lewis number

Figure Captions

Fig.1. Working geometry of expanding turbulent spherical flame (iso-contours of temperature distribution at 4 atm).

Fig. 2. DNS images of flame propagation (temperature iso-surfaces at flame front) in syngas/air mixtures at 4 atm, and at equivalence ratios of 0.7, 1.0 and 1.4, showing the development of cellular flame front instability for all three cases in high pressure environment.

Fig. 3. Iso-surfaces of flame front, coloured by local curvature values at 4 atm for equivalence ratios of 0.7, 1.0 and 1.4.

Fig. 4. Zoomed in figure, corresponding to the inset A of Fig. 3

Fig. 5. Probability density functions of local curvature at 4 atm for equivalence ratios of 0.7, 1.0 and 1.4.

Fig. 6. Thermo-diffusive (TD) instability, Darrieus-Landau (DL) instability, and growth rate as a function of wave number for equivalence ratios of 0.7, 1.0 and 1.4, showing the stabilisation of thermo-diffusive instability from lean to rich flames in high pressure environment.

Fig. 7. Spatial distribution of the HRR (showing cross-section of the full three-dimensional flame) for three equivalence ratios at a pressure of 4 atm.

Fig. 8. Zoomed in figure, corresponding to the inset A of Fig. 7

Fig. 9. Scatterplots of the HRR versus curvature along a flame front for three equivalence ratios at a pressure of 4 atm. Here the dashed-line shows the best-linear fitting curve.

Fig. 10. Scatter plots of normalised heat release rate with normalised HCO for three equivalence ratios at a pressure of 4 atm.

Fig. 11. Scatter plots of normalised heat release rate with normalised mass fractions product of OH and CH_2O for three equivalence ratios at a pressure of 4 atm.

Figures:

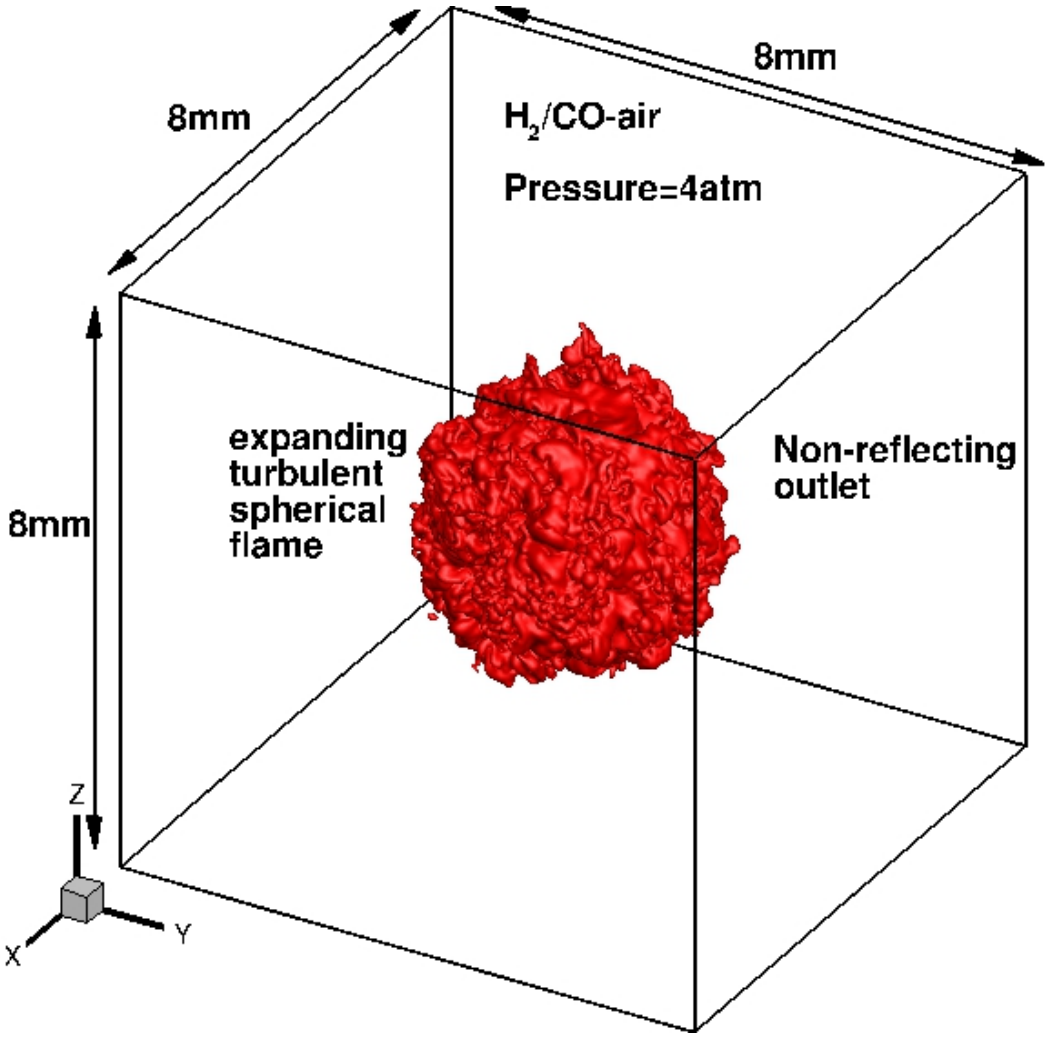

Fig.1. The computational configuration of the expanding turbulent spherical flame.

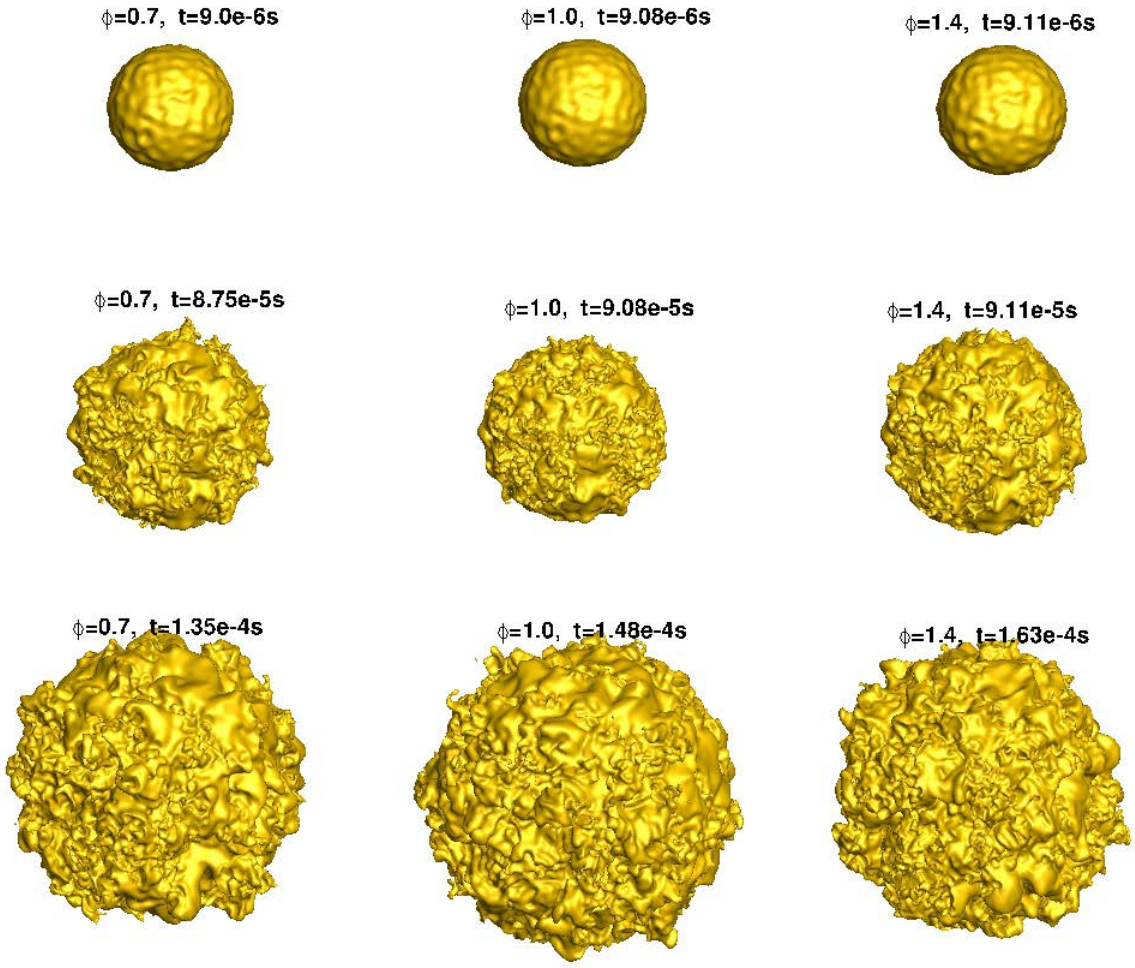

Fig. 2. DNS images of spherical flame growth (temperature iso-surfaces at flame front) in syngas/air mixtures at 4 atm at equivalence ratios of 0.7, 1.0 and 1.4, showing the development of cellular and wrinkled flame fronts for all the three cases at an elevated pressures.

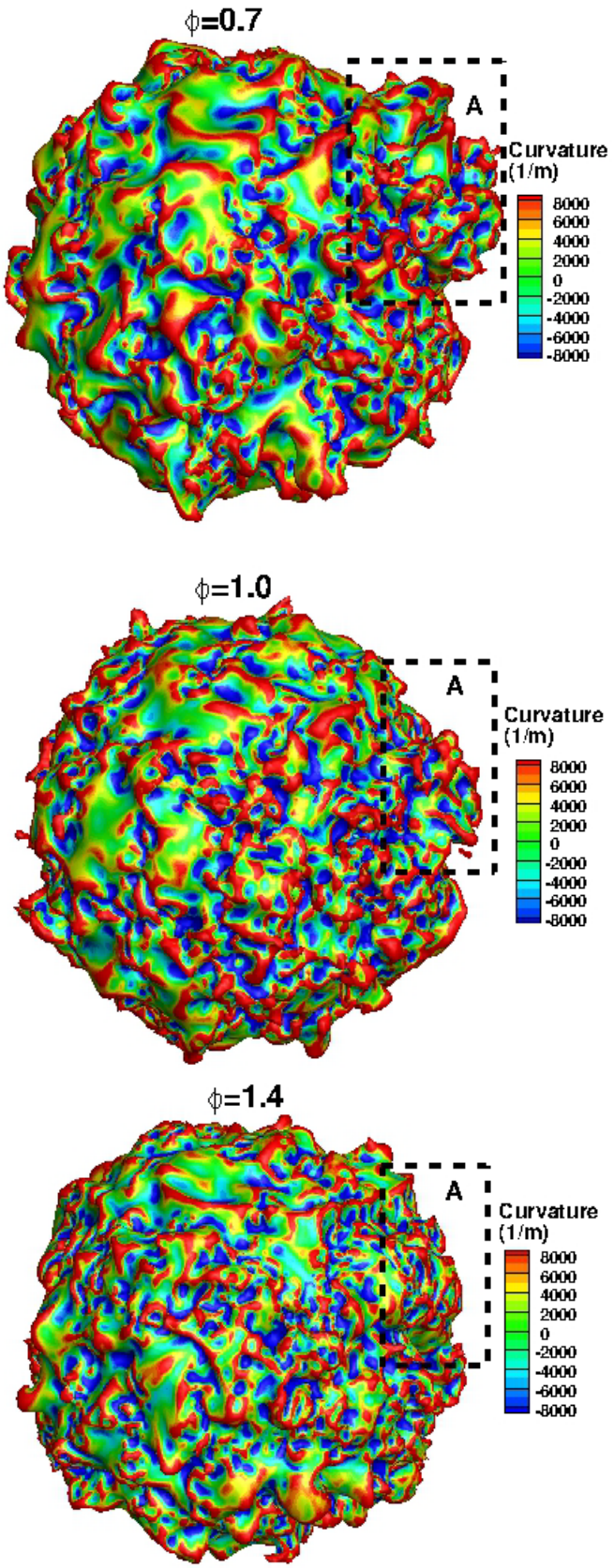
ϕ=0.7
A
Curvature
(1/m)
8000
6000
4000
2000
0
-2000
-4000
-6000
-8000
ϕ=1.0
A
Curvature
(1/m)
8000
6000
4000
2000
0
-2000
-4000
-6000
-8000
ϕ=1.4
A
Curvature
(1/m)
8000
6000
4000
2000
0
-2000
-4000
-6000
-8000

Fig. 3. Iso-surfaces of the flame front, coloured by local curvature values, at 4 atm for equivalence ratios of 0.7, 1.0 and 1.4.

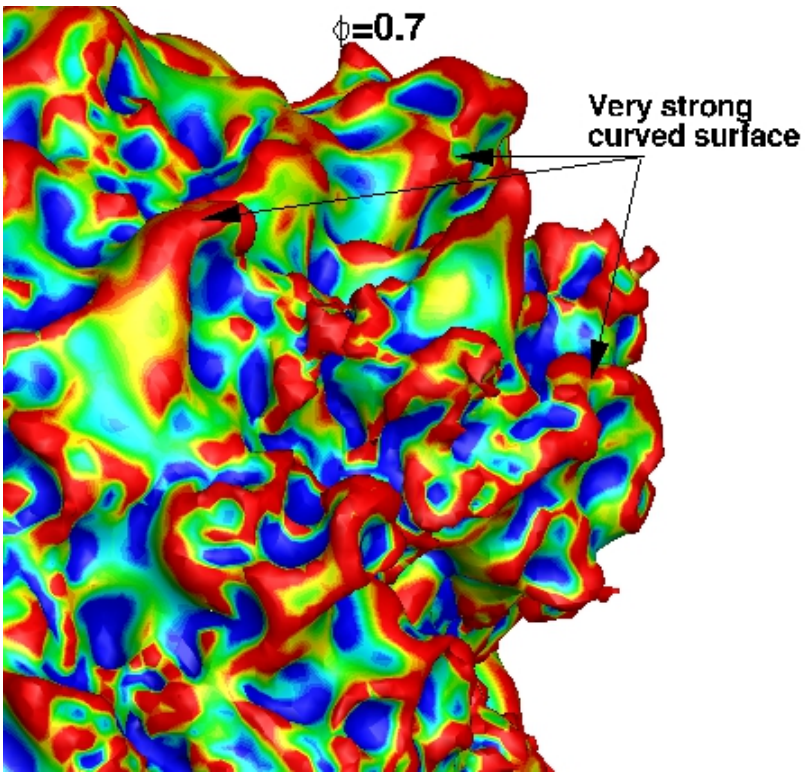

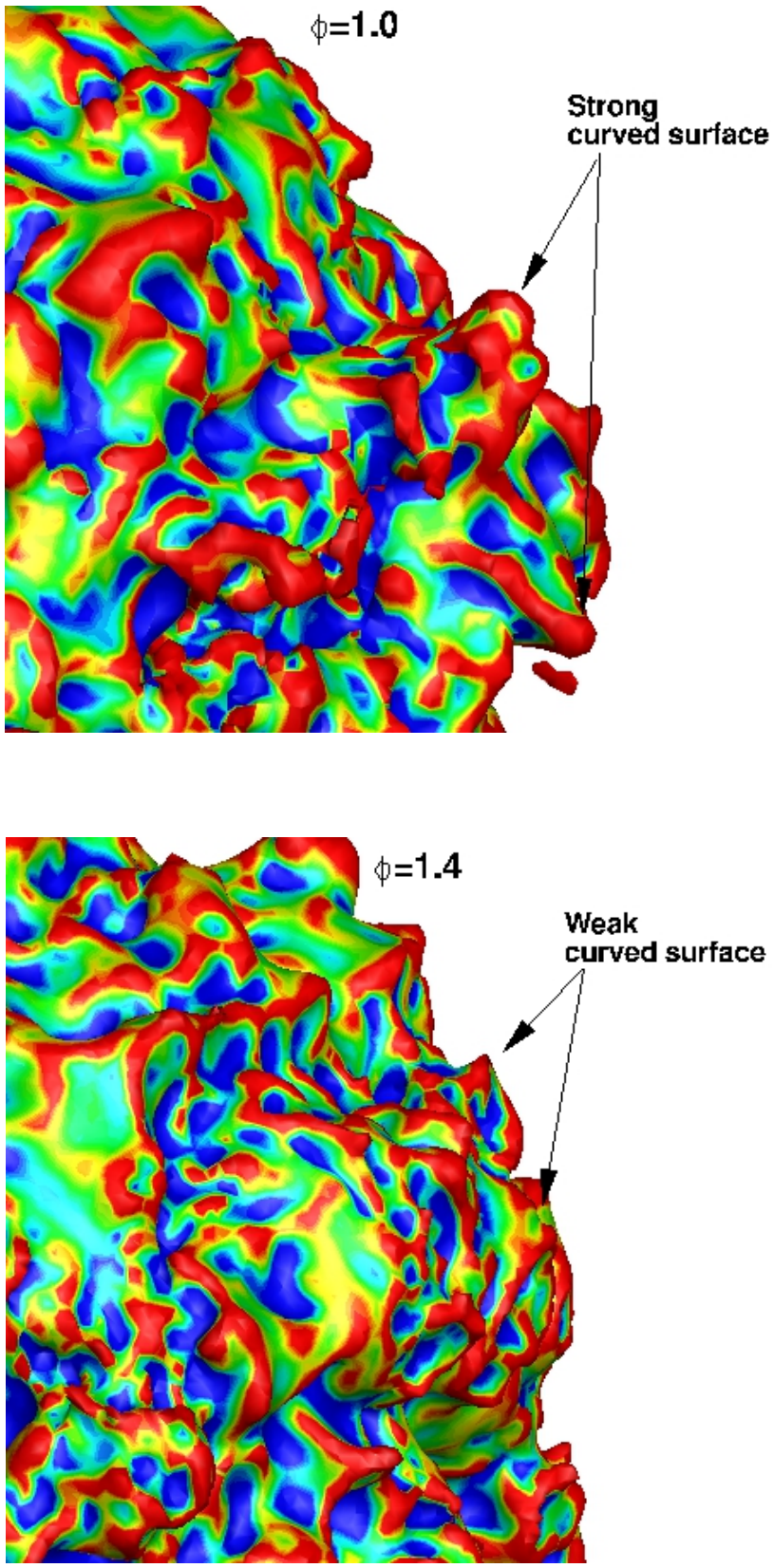

Fig. 4. Zoomed-in views, corresponding to the inset A of Fig. 3

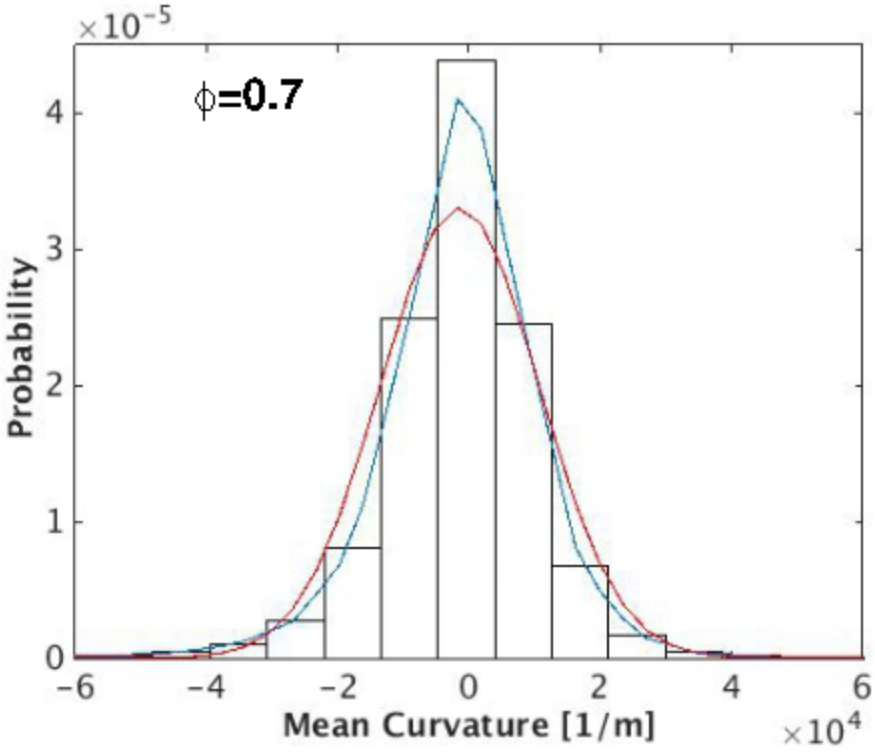
×10^-5
ϕ=0.7
Probability
Mean Curvature [1/m]
×10^4

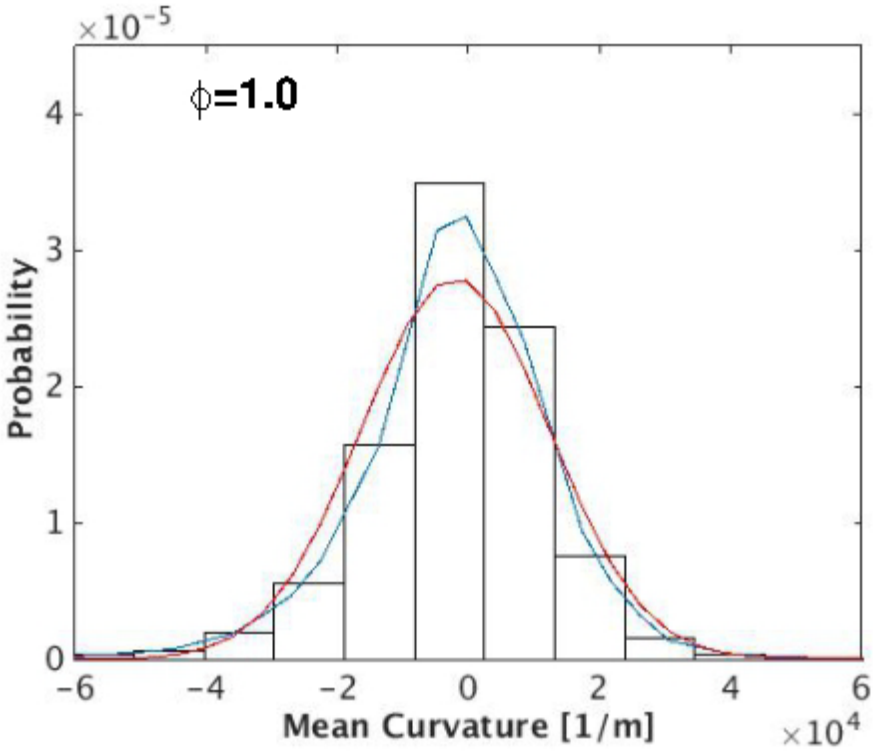
×10^-5
ϕ=1.0
Probability
Mean Curvature [1/m]
×10^4

(b)

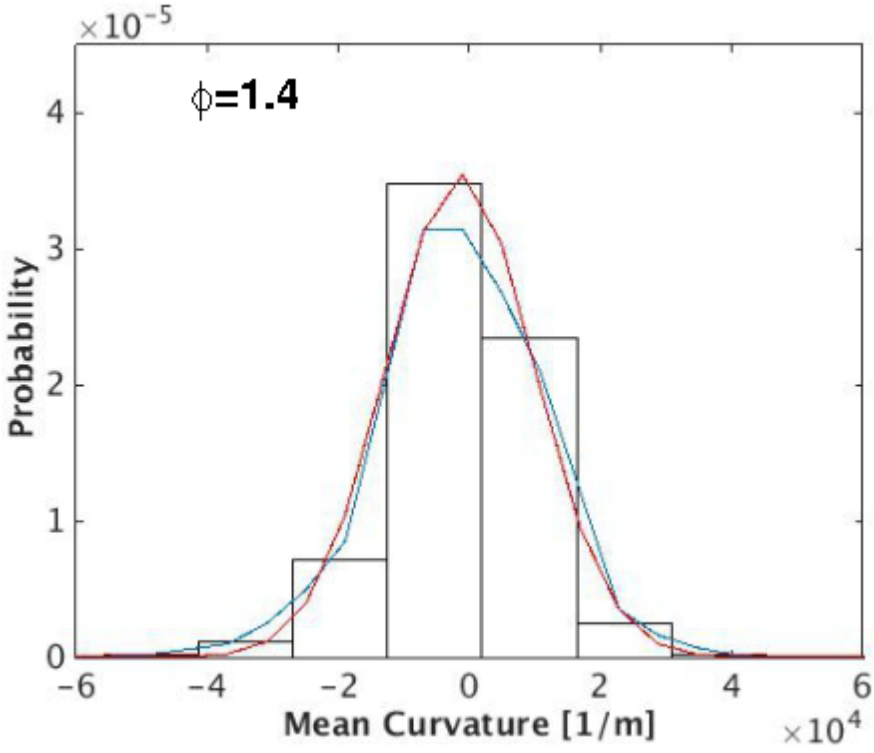
×10^-5
ϕ=1.4
Probability
Mean Curvature [1/m]
×10^4

Fig. 5. Probability density functions of local curvature at the flame front at 4 atm for equivalence ratios of 0.7, 1.0 and 1.4.

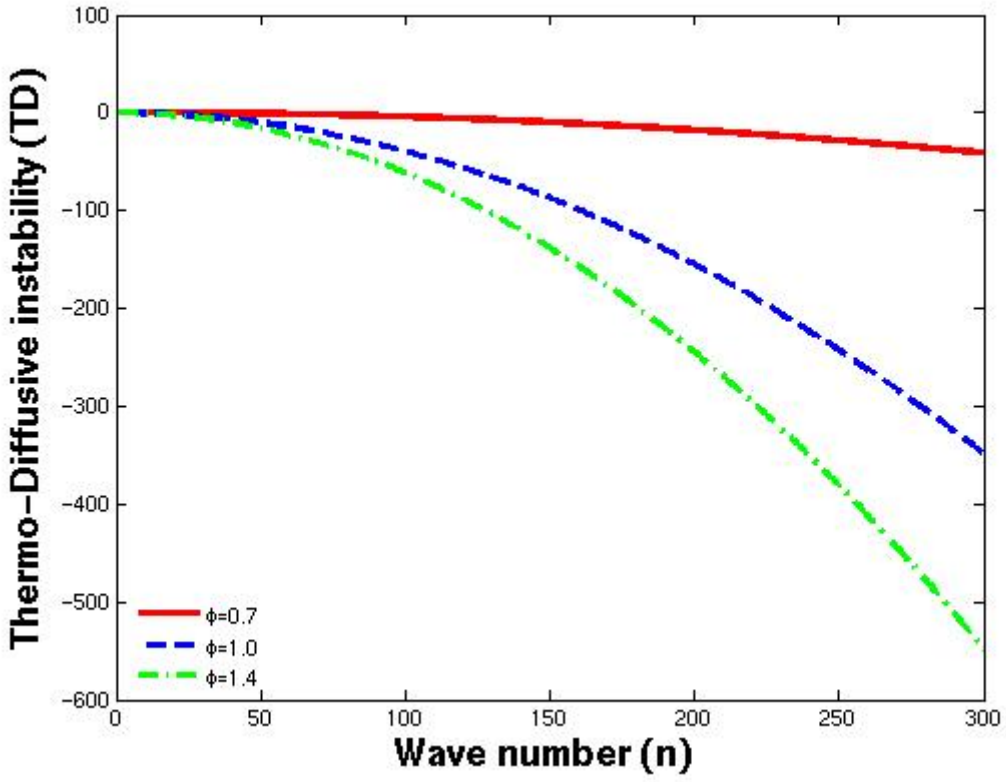

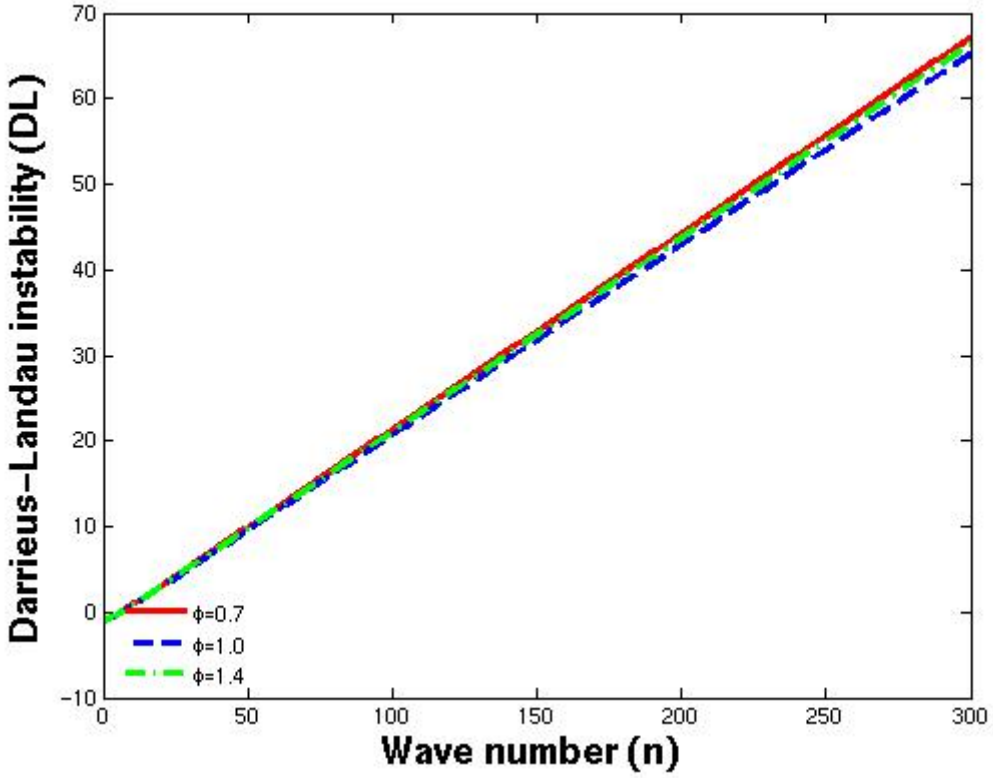
Darrieus–Landau instability (DL)
Wave number (n)
ϕ=0.7
ϕ=1.0
ϕ=1.4
70
60
50
40
30
20
10
0
−10
0
50
100
150
200
250
300

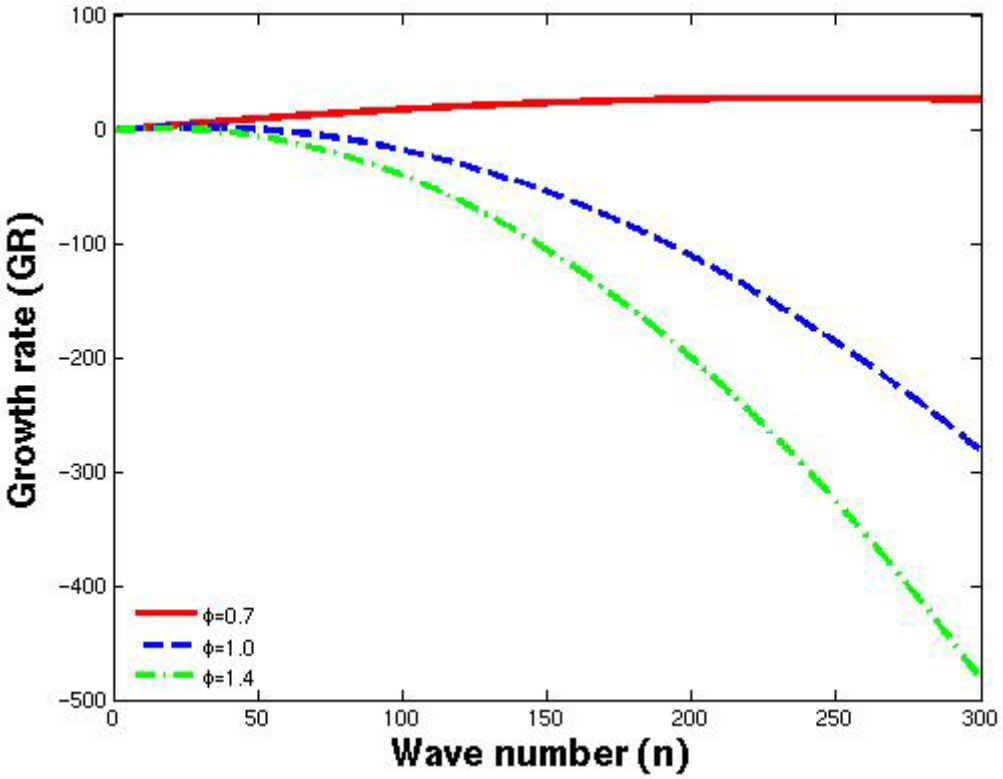
Growth rate (GR)
Wave number (n)
ϕ=0.7
ϕ=1.0
ϕ=1.4
100
0
−100
−200
−300
−400
−500
0
50
100
150
200
250
300

Fig. 6. Thermo-diffusive (TD) effect, Darrieus-Landau (DL) instability, and growth rate as a function of the wave number for equivalence ratios of 0.7, 1.0 and 1.4, showing thermo-diffusive stabilising effect increasing from lean to rich flames at an elevated pressure.

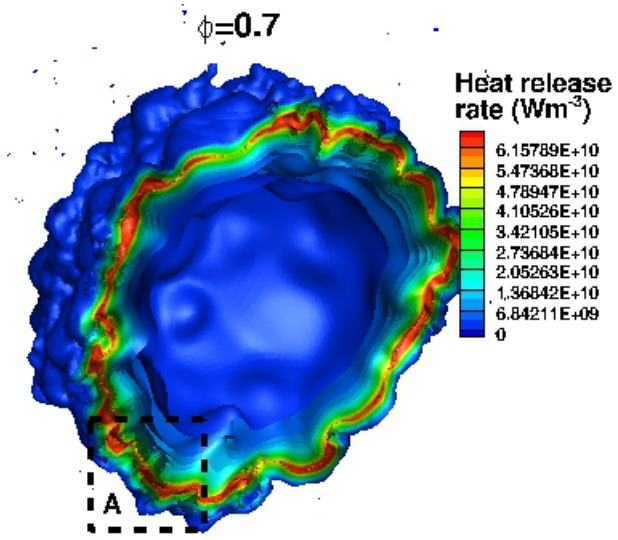

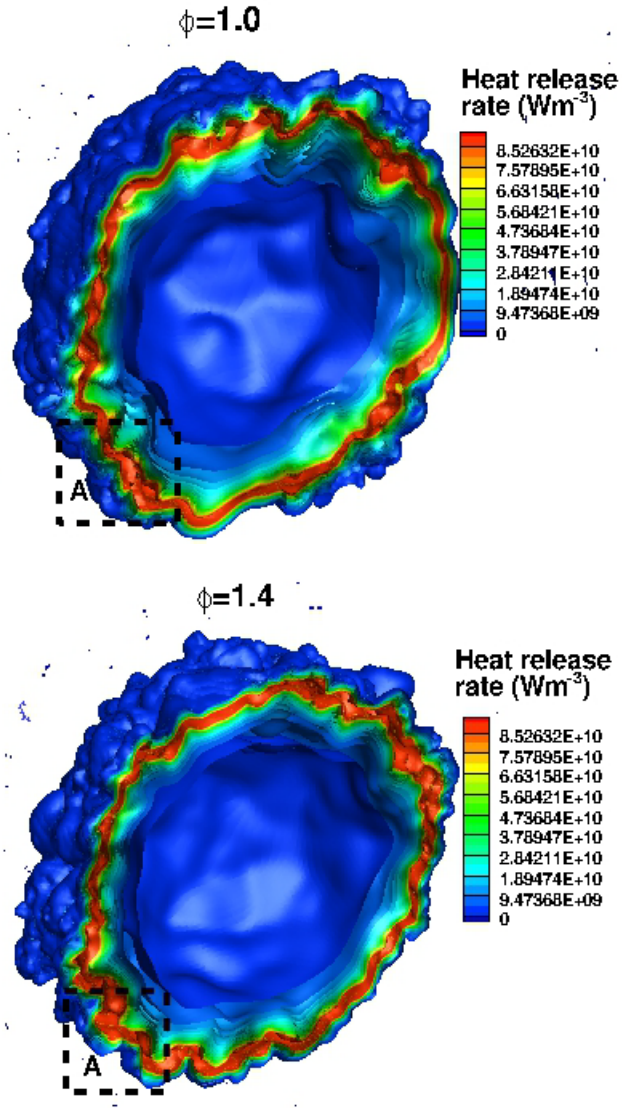

Fig. 7. Spatial distribution of the heat release rate (HRR) in a cross-section of the full three-dimensional flame ball for three equivalence ratios at a pressure of 4 atm.

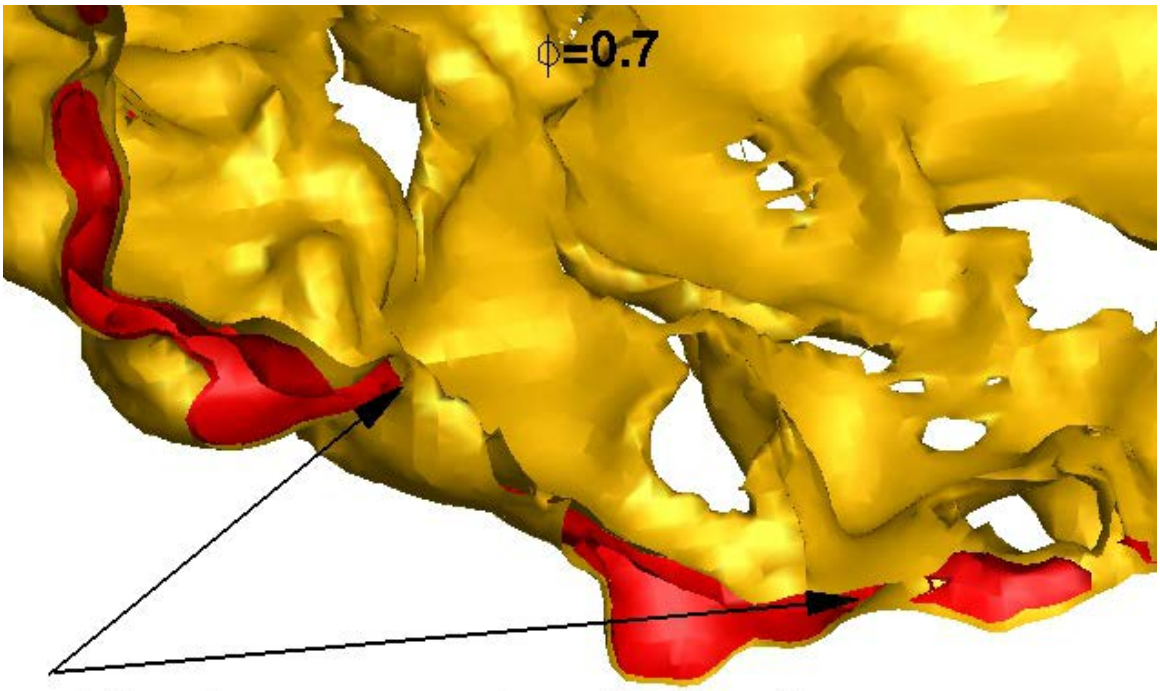

weak burning structures along the flame front

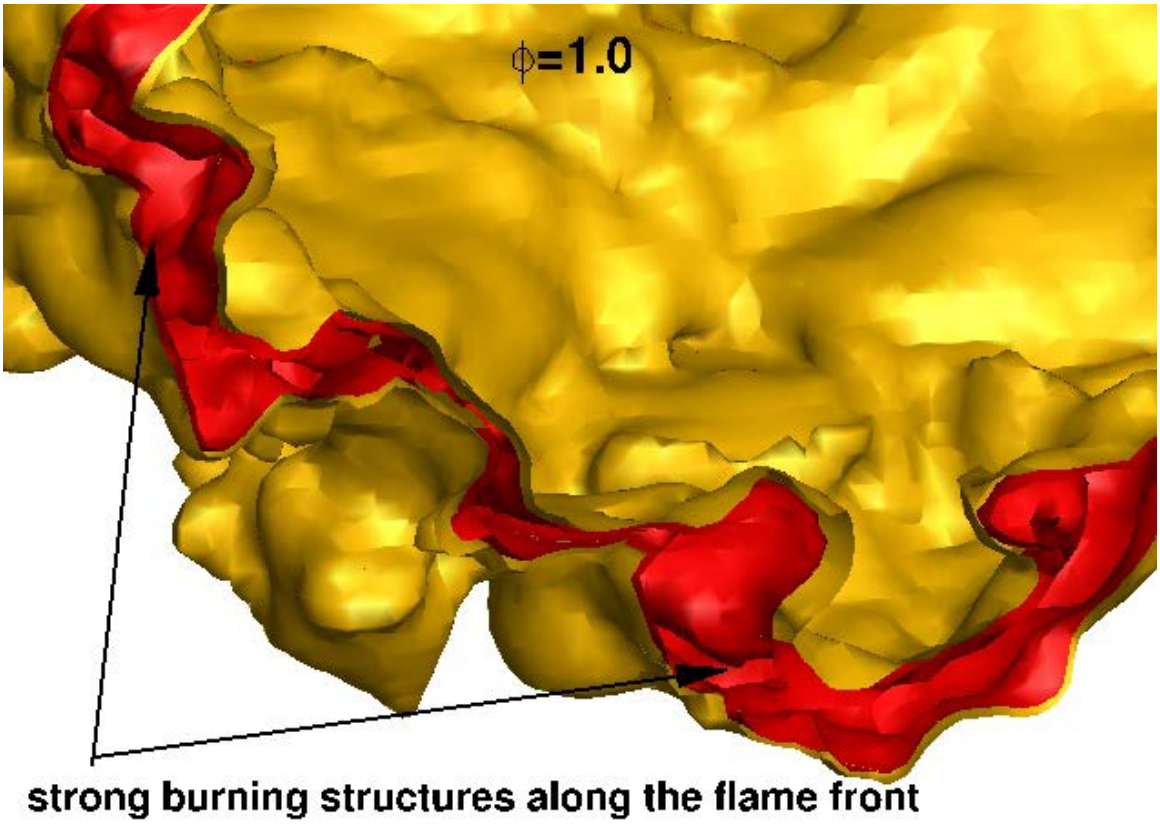
ϕ=1.0
strong burning structures along the flame front

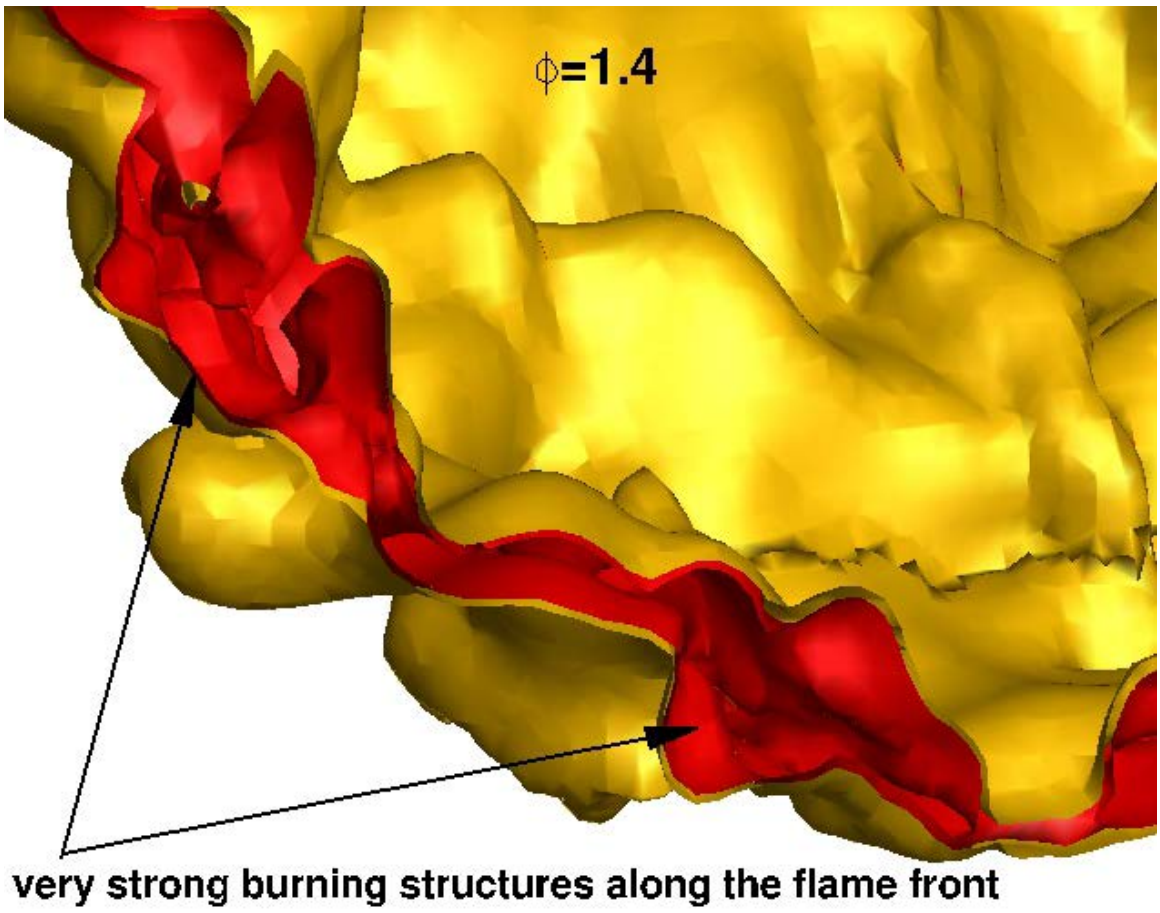

Fig. 8. Zoomed-in views, corresponding to the inset A of Fig. 7

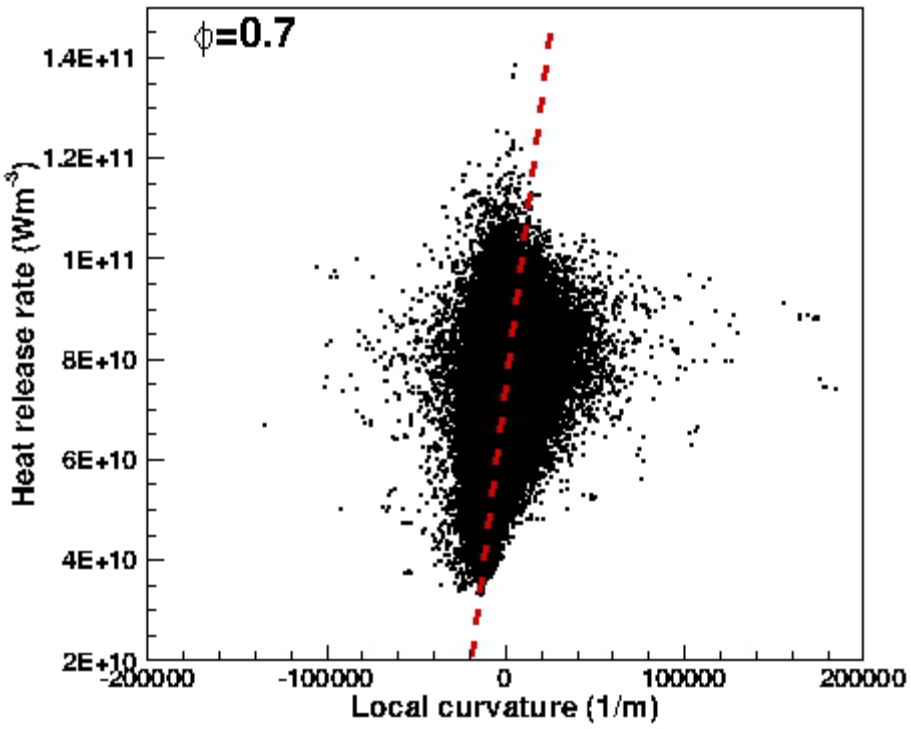
ϕ=0.7
Heat release rate (Wm-3)
1.4E+11
1.2E+11
1E+11
8E+10
6E+10
4E+10
2E+10
-200000
-100000
0
100000
200000
Local curvature (1/m)

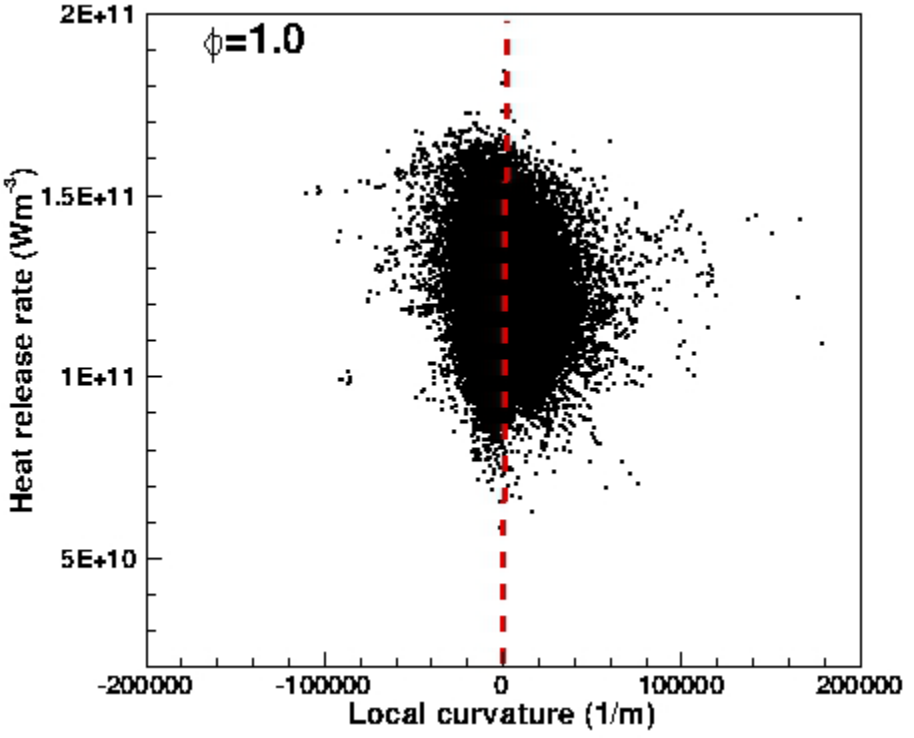
ϕ=1.0
Heat release rate (Wm-3)
2E+11
1.5E+11
1E+11
5E+10
-200000
-100000
0
100000
200000
Local curvature (1/m)

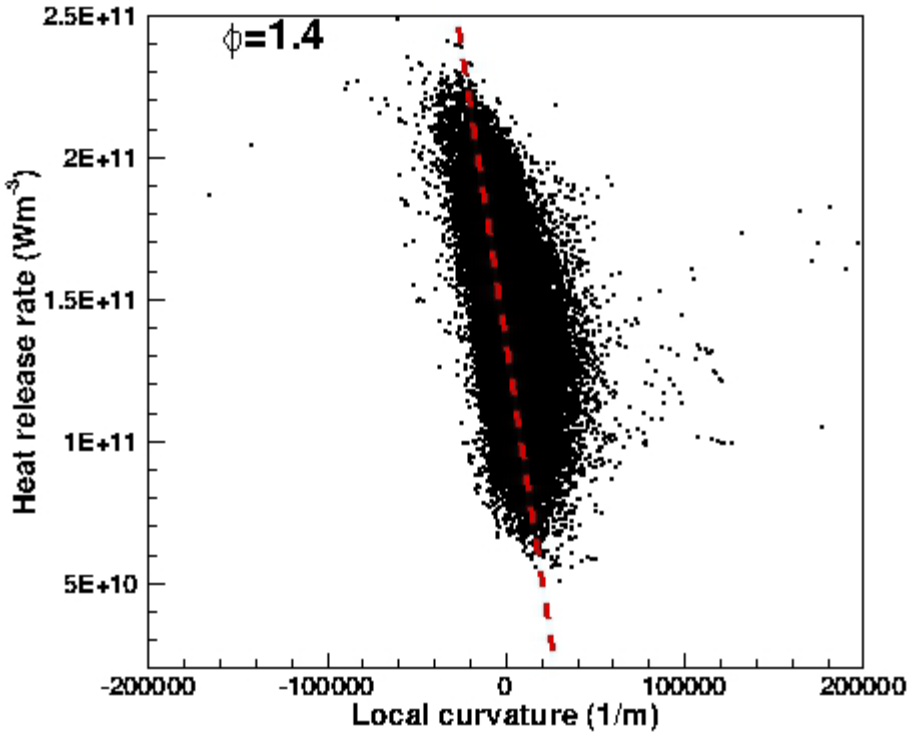

Fig. 9. Scatter plots of the HRR versus curvature along the flame front for three equivalence ratios at a pressure of 4 atm. Here the dashed-line shows the best-linear fitting curve.

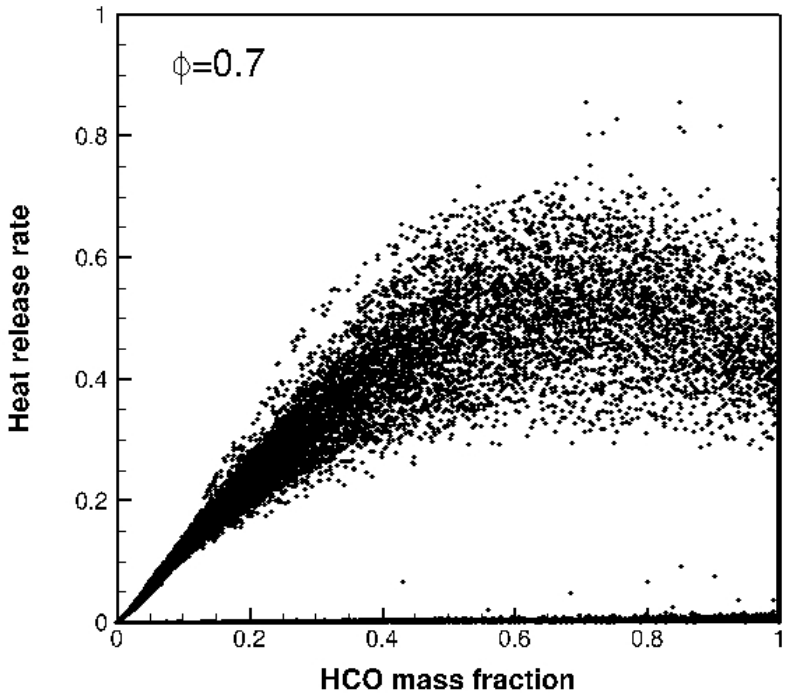
ϕ=0.7
Heat release rate
HCO mass fraction
0
0.2
0.4
0.6
0.8
1

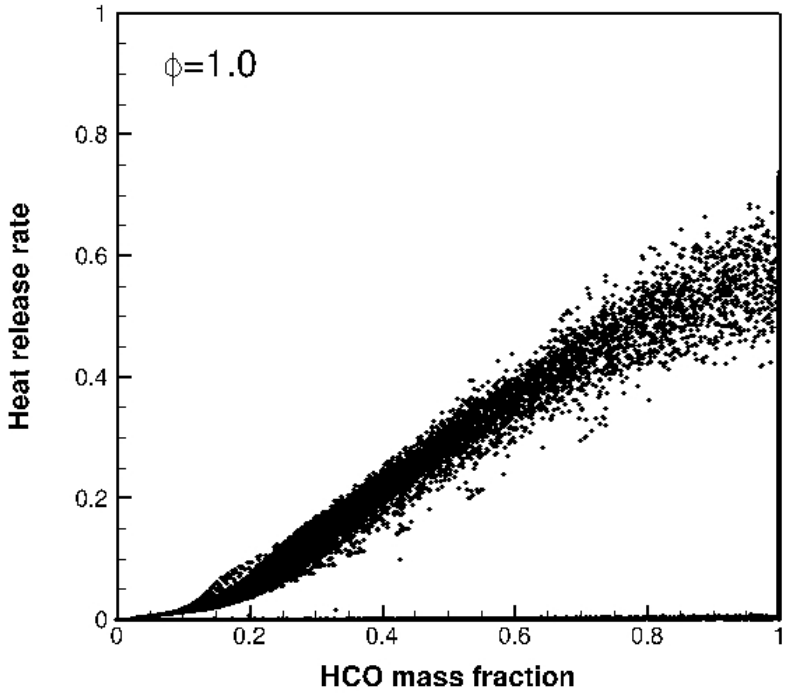
ϕ=1.0
Heat release rate
HCO mass fraction
0
0.2
0.4
0.6
0.8
1

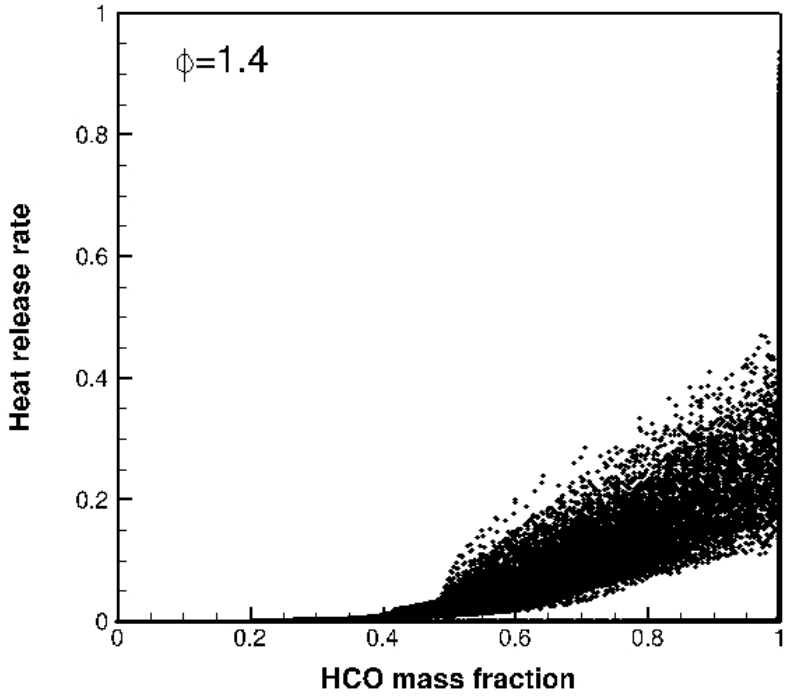

Fig. 10. Scatter plots of normalised heat release rate with normalised HCO for three equivalence ratios at a pressure of 4 atm.

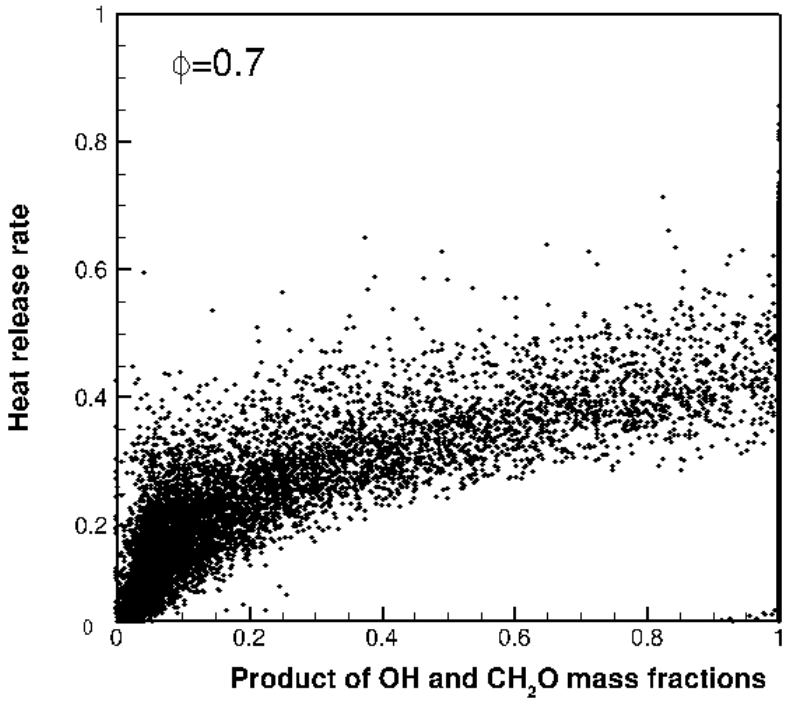
ϕ=0.7
Heat release rate
Product of OH and CH2O mass fractions
0
0.2
0.4
0.6
0.8
1

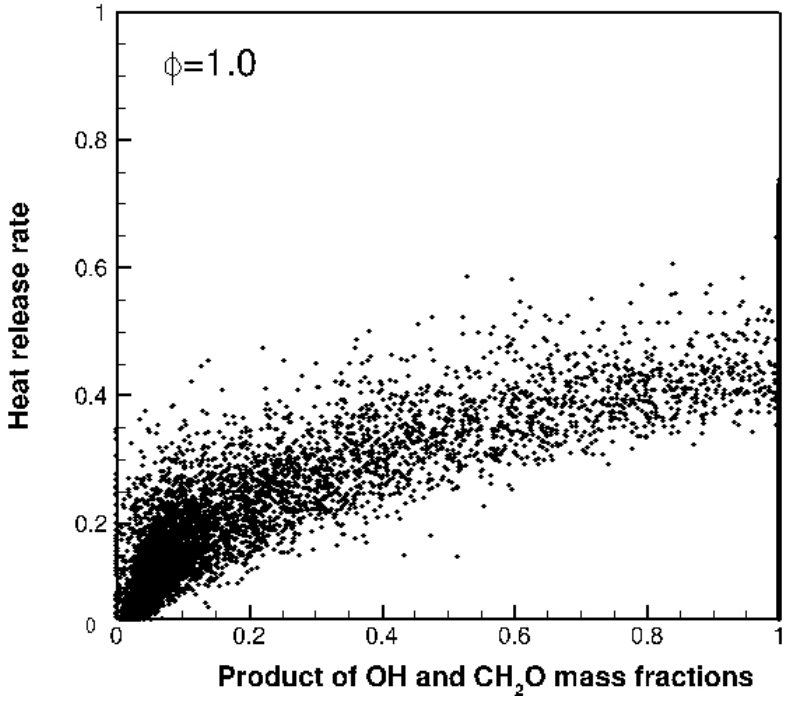
ϕ=1.0
Heat release rate
Product of OH and CH2O mass fractions
0
0.2
0.4
0.6
0.8
1

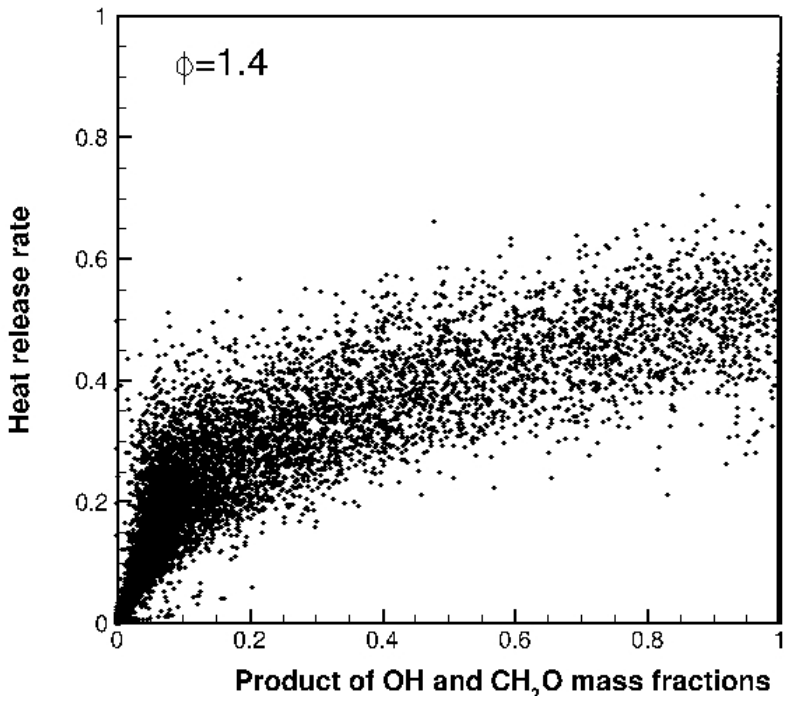

Fig. 11. Scatter plots of normalised heat release rate with normalised mass fractions product of OH and CH_2O for three equivalence ratios at a pressure of 4 atm.